The Thesis Committee for Daniel Armin Enriquez
Certifies that this is the approved version of the following thesis:

Methane Resaturation in Barnett Formation Core Plugs and Determination of Post-coring Gas Loss

APPROVED BY
SUPERVISING COMMITTEE:

Supervisor:

Charles Kerans

Co-supervisor:

Tongwei Zhang

William L. Fisher

Scott W. Tinker

Methane Resaturation in Barnett Formation Core Plugs and Determination of Post-coring Gas Loss

by

Daniel Armin Enriquez, B.S.

Thesis

Presented to the Faculty of the Graduate School of

The University of Texas at Austin

in Partial Fulfillment

of the Requirements

for the Degree of

Master of Science in Geological Science

The University of Texas at Austin

May 2017

Dedication

I would like to dedicate this thesis to my father, Ruben Enriquez Sr., mother, Marisela Wheeler, and brother, Ruben Enriquez Jr. Without the love and support of all three of you this thesis and my education would not have been possible.

Acknowledgements

This master's thesis is the successful result of research conducted within, and financially supported by, the Mudrocks Systems Research Laboratory consortia at the Bureau of Economic Geology, Jackson School of Geosciences, the University of Texas at Austin, Austin, TX and the Shaanxi Yanchang Petroleum (Group) Co. Thanks, gratitude, and appreciation are directed to all of MSRL's sponsors: Anadarko, Apache, Aramco Services, BHP Billiton, BP, Cenovus, Centrica, Chesapeake, Cima, Cimarex, Chevron, Concho, ConocoPhilips, Cypress, Devon, Encana, ENI, EOG, EXCO, ExxonMobil, FEI, Geosun, Hess, Husky, IMP, Kerogen, Marathon, Murphy, Newfield, Oxy, Penn West, Penn Virginia, Pioneer, QEP, Repsol, Samson, Shell, Sinopec, StatOil, Talisman, Texas American Resources, The Unconventionals, University Lands, US EnerCorp, Valence, and YPF.

First and foremost I would like to thank my entire family for their continuous love and support through not only the past two years of graduate school, but for their encouragement and fostering of my higher education from an early age. I would like to thank and show appreciation toward my mentor and supervisor Dr. Tongwei Zhang for all of the opportunities he has presented me with during my time working for and with him over the past three years. Special thanks are given to my dear friend and colleague Dr. Xun Sun, and the numerous visitors from Yanchang Petroleum and the various other Chinese institutions who I have had the pleasure of meeting and befriending. Many thanks and well wishes go out to everyone at the Bureau of Economic Geology, and my close friends over at the Core Research Center, Nathan Ivicic, Brandon Williamson, Bill Molthen, and Rudy Lucero.

I would also like to thank my advisor Dr. Charles Kerans, my committee members Dr. Scott W. Tinker and Dr. William L. Fisher, and my good friends and staunchest supporters Eric C. Potter. Special thanks go out to Richard E. Newhart, Thomas M. Smagala, Mark H. Tobey, and Kyle E. Gorynski for providing me with the opportunity to commence my professional career as a geologist at Encana Corporation. This amazing group of people have supported me, lent a hand, and given advice throughout my entire tenure here at the University of Texas, and for the future.

Abstract

Methane Resaturation in Barnett Formation Core Plugs and Determination of Post-coring Gas Loss

Daniel Armin Enriquez, M.S. Geo. Sci.

The University of Texas at Austin, 2017

Supervisor: Charles Kerans, Tongwei Zhang

Understanding the physiochemical mechanisms that control the loss of gas during coring processes is critical to accurately determining gas-in-place (GIP) resource assessments of unconventional shale-gas plays. Our study uses an experimental approach, utilizing methane (CH_4) adsorption isotherms and degassing curves of methane-resaturated Barnett Formation core plugs, to determine the amount of lost-gas based on mass-balance analysis at different CH_4 re-saturation pressures and varied exposure times. Several readily available empirical methods for estimating lost-gas were evaluated, quantified, and compared with the mass balance–derived lost-gas values in our experiments.

A CH_4 isotherm measurement on 3/8-inch Barnett Formation core plugs was performed at 35.4°C; the amount of gas adsorbed was then quantified and fitted to the modified Langmuir equation to determine the Langmuir maximum, Langmuir constant, and adsorbed gas-phase density. Two sets of CH_4 gas-resaturation and degassing

measurements, one varying saturation pressures and the other varying exposure times, were performed on 3/8-inch Barnett Formation core-plugs at an isothermal temperature of 35.4°C. Degassing curves, the plot of the released gas yield versus the square root of degassing time, display three stages that correspond to different gas-releasing mechanisms. The rapid increase of released gas yield at the beginning of degassing represents that linear gas expansion is dominant and that degassing evolves into a nonlinear desorption-dominated phase over time. Experimentally derived values for lost gas were determined by subtracting the sum of the emitted and retained gas at the peak of the degassing curve from the amount of gas initially charged into the samples at equilibrated resaturation pressure. Lost gas varies linearly with increasing gas-resaturation pressure and nonlinearly by a greater magnitude with increasing exposure time, indicating that lost gas is more sensitive to exposure time.

The uncertainty evaluation of lost gas determined by three empirical methods was conducted by direct comparison with mass-balance-derived lost-gas values from our experiment. Nonlinear least-squares extrapolation overestimates, and both linear extrapolation and polynomial equation fitting underestimate, mass-balance lost-gas control points. Among the three empirical methods, the polynomial-fitted lost-gas values most closely agree with mass-balance lost gas, revealing that polynomial fitting to degassing curves is a viable way to accurately estimate lost gas and, more importantly, to estimate GIP values with up to 85% accuracy.

Table of Contents

Chapter 1: Introduction

Within the past 15 years, gas production from shale-gas reservoirs has become a significant source of domestic energy, and is viewed as a key strategic resource in terms of current and future energy security, energy production, and energy consumption. Natural-gas production from shales continues to increase throughout the United States, making up roughly 55% of total natural-gas production in 2016, and is projected to account for up to 66% of total natural-gas production by 2040 (EIA, 2017). Current natural-gas consumption in the United States is expected to rise by nearly 17% over the next 23 years, and shale gas is estimated to account for upward of one-third of all energy consumed nationwide by 2040 (EIA, 2017).

The proliferation of unconventional reservoir plays, with their considerable amounts of reserves and production, have incentivized the need for accurate in situ gas-in-place (GIP) assessments that take generation, migration, and retention into account for further investment and development. Gas storage within shale-gas reservoirs is inherently unique and complex compared to other unconventional reservoirs because gas is stored in the form of free gas compressed into the pore volume and adsorbed gas that adheres to pore surfaces (Zhang and Krooss, 2001; Javadpour, 2009; Loucks et al., 2009; Zhang et al., 2012; Etminan et al., 2013; Gasparik et al., 2013; Milliken et al., 2013; Hosseini et al., 2015, Hu et al., 2015). Due to this added gas-storage complexity, understanding in situ GIP volumes and gas deliverability is critical when attempting to assess the risks and

economics associated with exploration, production, reserve estimation, and field design for unconventional shale-gas plays.

In situ GIP is currently estimated through utilization of one of two distinct methods: (1) pressure coring, or (2) canister desorption (degassing). Pressure coring involves an operator coring a formation and immediately preserving the core, at depth and under in situ conditions, within special containers that prevent the escape of reservoir fluids during core retrieval and handling (Mullane, 1941; Hyland, 1983; Mavor et al., 1994; Seidle, 2011). Canister-desorption techniques include traditionally coring a formation, transporting core up the borehole, and immediately placing select sections into airtight canisters whose pressures are monitored over time (Bertard et al., 1970; Kissell et al., 1973; Yee et al., 1993; McLennan et al., 1995; Diamond and Schatzel, 1998; Waechter and Hampton, 2004; Seidle, 2011). Pressure coring directly quantifies fluids in place and is significantly more expensive than canister-desorption methods. Routinely, the canister-desorption technique is used to estimate GIP based on the sum of canister released gas, retained gas, and lost gas. Lost-gas estimation is problematic because of depressurization experienced by cores during borehole transport and surface handling.

The estimation of gas lost during core transport and handling is critical when performing a GIP estimation using the canister-desorption technique. Quantification of lost gas typically involves the empirical fitting of various mathematical functions to measured canister-degassing curves and extrapolating backward to the origin using a multitude of empirical techniques. Canister desorption and these empirical techniques, pioneered for use in the coalbed methane (CBM) industry between the 1970's and

1990's, have only recently been applied to organic-rich shale-gas plays. Compared to CBM, various studies and industry practices that utilize this empirical methodology have done so with little regard for the differing mechanisms that control gas storage and release in organic-rich shale-gas reservoirs. While simple, these empirical techniques are not consistent and have the inherent downside of producing different estimations for lost gas depending on which function is fitted or which extrapolation technique is used.

To address the shortcomings of canister desorption, accurately determine lost gas, and examine the key mechanisms affecting gas loss, we developed an experimental method that would allow the simulation of the types of pressures experienced by cored samples during the coring, transport, and handling process. Our experimental method utilized core-plug samples as the best approximation of in situ reservoir conditions. A mass-balance methodology was employed to accurately quantify the amount of gas lost from our samples during a constrained period of exposure; results were then compared to the results of lost gas determined by various empirical methods. This comparison, between our experimentally determined control points and varying empirically derived lost-gas estimations, allowed for evaluating which empirical methodology is most valid for use in GIP assessments, presuming our method is reasonably accurate.

To address this question, the primary objectives of this study are to (1) develop an experimental method combining isothermal methane resaturation of core plugs with CH_4 adsorption isotherms in order to measure lost gas; (2) examine the key factors controlling gas loss, specifically core exposure time and initial CH_4 resaturation pressure to gas loss in post coring; and (3) build a model based upon present degassing mechanisms and

mass-balance calculations to more accurately predict post-coring gas loss and better estimate GIP.

This body of work has helped resolve several questions that have puzzled academic and industry geochemists, as well as geologists, who assess shale-gas resources. The key contribution and findings that have been made from this study include:

(1) The creation of a well-constrained experimental methodology that simulates reservoir, transport, and surface handling pressure conditions has allowed for an accurate mass-balance-derived quantification of gas loss during an exposure period for the first time.

(2) The effective pore volume available for free gas storage was determined and practically applied to our mass-balance calculations due in part to obtaining a reliable adsorbed CH_4 isotherm using core plugs.

(3) Solid experimentally-derived evidence was also gained into the different gas releasing mechanisms which affect organic-rich shale-gas loss over time. A combination of gas expansion and desorption were determined to be the two main attributable degassing mechanisms.

(4) An uncertainty evaluation of estimated gas loss values, based on three empirical CBM industrial methods, clearly validated the polynomial fitting method as the best overall analyzed empirical methodology for determining lost gas in organic-rich shales.

Chapter 2: Geologic Background

OVERVIEW OF THE FORT WORTH BASIN AND BARNETT FORMATION

The Mississippian-aged Barnett Formation is an organic-rich shale-gas mudrock system deposited within the Fort Worth Basin (Figure 1) of north-central Texas during the late Paleozoic Ouachita orogeny (Walper, 1982; Jarvie et al., 2005; Montgomery et al., 2005; Jarvie et al., 2007; Loucks and Ruppel, 2007; Pollastro et al., 2007; Rowe et al., 2008; Loucks et al., 2009). The Fort Worth Basin (FWB) is bordered by the Red River and Muenster Arches to the north, the Llano Uplift to the south, the Bend Arch to the west, and the Ouachita thrust–fold belt to the east (Figure 1) (Montgomery et al., 2005; Jarvie et al., 2007; Loucks and Ruppel, 2007; Pollastro et al., 2007; Rowe et al., 2008). Several different plate reconstructions suggest the FWB "occupied a narrow inland seaway between the rapidly approaching continents of Laurussia and Gondwana" during the progression of the Ouachita orogeny (Gutschick and Sandberg, 1983; Arbenz, 1989; Blakey, 2005; Loucks and Ruppel, 2007; Rowe et al., 2008).

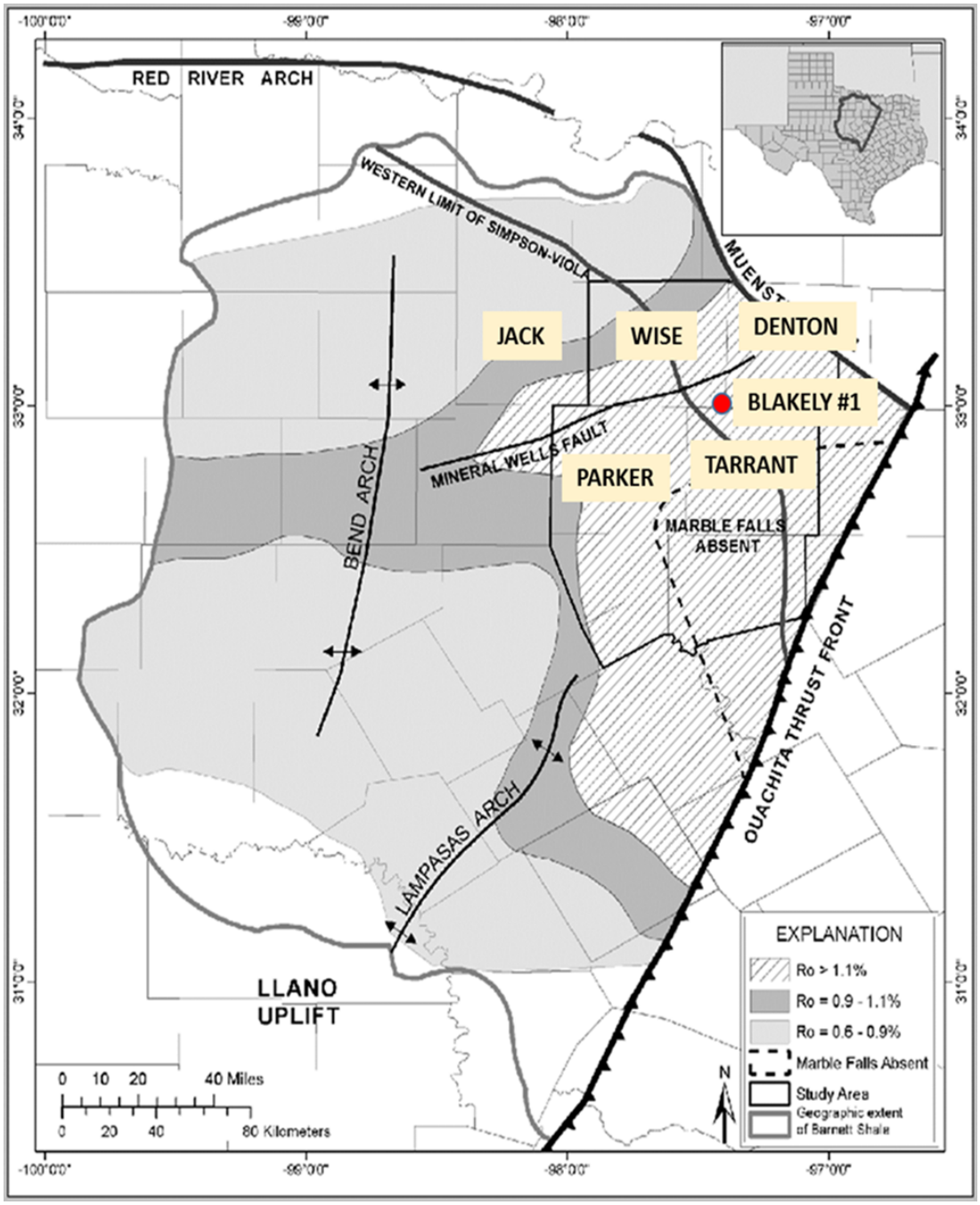

Figure 1. Map of Fort Worth Basin, including county names and location of Texas United Blakely #1 well. Modified from Fu et al. (2015).

The Barnett Formation of the FWB is one of the premier organic-rich shale-gas plays in North America in terms of natural-gas production (1.6 Tcf) and proven reserves (53 Tcf) (Browning et al., 2013; EIA, 2015; Fu et al., 2015; USGS, 2015; RRC, 2017). The Barnett Formation can be classified as a shale-gas system that simultaneously features the rock as a combination self-sourced reservoir and seal (Loucks and Ruppel, 2007). Thin-section analysis in combination with XRD analysis of the Barnett formation by Loucks and Ruppel (2007) reveals that quartz (34.3%), dominantly illite and minor smectite clays (24.2%), calcite of various forms (16.1%), pyrite (9.7%), and feldspar (6.6%) form the bulk of the Barnett Formation mineral matrix. Minor amounts of dolomite and ankerite (5.6%), phosphate minerals (3.3%), and trace amounts of siderite (0.3%) compose the remaining matrix portion of the Barnett (Loucks and Ruppel, 2007). The Barnett Formation is unconformably underlain by Ordovician-aged carbonates of the Ellenburger Group and Viola Formation, and is conformably overlain by the Pennsylvanian-aged lower Marble Falls Formation (Loucks and Ruppel, 2007; Rowe et al., 2008). The carbonate-rich Forestburg limestone is recognized to separate the Barnett Formation into upper and a lower section throughout a majority of the FWB (Montgomery et al., 2005; Jarvie et al., 2007; Loucks and Ruppel, 2007; Pollastro et al., 2007).

The deposition of the Barnett Formation is recognized to have occurred in water depths of 120 to 215 m, below storm-wave base and below the oxygen minimum zone, under anoxic to euxinic water-column conditions (Loucks and Ruppel, 2007; Rowe et al., 2008). Water-column stratification within the FWB during Barnett Formation deposition

was due to highly restricted oceanic circulation conditions (Loucks and Ruppel, 2007; Rowe et al., 2008). The restriction of oceanic circulation results from the combination of the narrow and deep foreland geometry of the FWB along with poor connection of the basin with the open ocean (Loucks and Ruppel, 2007; Rowe et al., 2008). Deposition of the Barnett Formation is observed to have occurred during a second-order sea-level highstand over an approximately 25-million-year time period (Loucks and Ruppel, 2007; Rowe et al., 2008). The major depositional processes for the Barnett Formation can be characterized as suspension settling, debris flows, contourites, and turbidity currents (Loucks and Ruppel, 2007). As a result of the euxinic to anoxic bottom-water conditions and a lack of living biota in the deep FWB, organic-matter content within the Barnett Formation is considered high (3.3–13 wt % total organic carbon [TOC]) and optimal for hydrocarbon production (Jarvie et al., 2001, 2005; Loucks and Ruppel, 2007). Original TOC of the Barnett Formation is estimated to be as high as 20 wt % (Bowker, 2003; Loucks and Ruppel, 2007).

The thickness of the Barnett Formation ranges from 30 to 50 ft in exposed outcrops in Llano, Lampasas, and San Saba Counties in the southwestern portion of the FWB to more than 1,000 ft thick adjacent to the Muenster Arch in Denton and Cooke Counties (Cheney, 1940; Plummer, 1950; Montgomery et al., 2005). Burial-history reconstructions proposed by Jarvie et al. (2001) and Montgomery et al. (2005) suggest a three-phase burial history for the Barnett Formation. These three stages encompass (1) a period of rapid subsidence between the Pennsylvanian and Permian (~300–250 Ma), (2) a period between the Late Permian and Early Cretaceous (~250–140 Ma) characterized

overall by elevated temperatures with a minor increase in burial from the middle to Late Cretaceous (~140–100 Ma), and (3) a period of rapid uplift and overburden removal from the Late Cretaceous to the mid-Paleocene (~100–40 Ma) (Jarvie et al., 2001; Montgomery et al., 2005). As a result of this multistage thermal history, the thermal maturity of the Barnett ranges from immature (0.48% RO) in the northwest portion of the basin to within the gas window (2.64% RO) in the southeast portion (Jarvie et al., 2001, 2003, 2005, 2007; Montgomery et al., 2005).

TEXAS UNITED BLAKELY #1 CORE WELL

The Texas United Blakely #1 was cored in 1981 from within the Newark–East core area of the Barnett Formation in southeastern Wise County, Texas. The cored section of the Blakely #1 spans 120 ft of uninterrupted core throughout the upper Meramecian and lower Chesterian stages of the Barnett Formation (345–318 Ma) (Figure 2). The difference between the spectral and cumulative gamma ray logs suggests high organic-matter content in the upper and lower Barnett sections compared to that of the Forestburg limestone. Three distinct lithofacies—skeletal argillaceous lime packstones, nonlaminated to laminated siliceous mudstones, and laminated argillaceous lime marls—are observed for the Barnett Formation (Loucks and Ruppel, 2007).

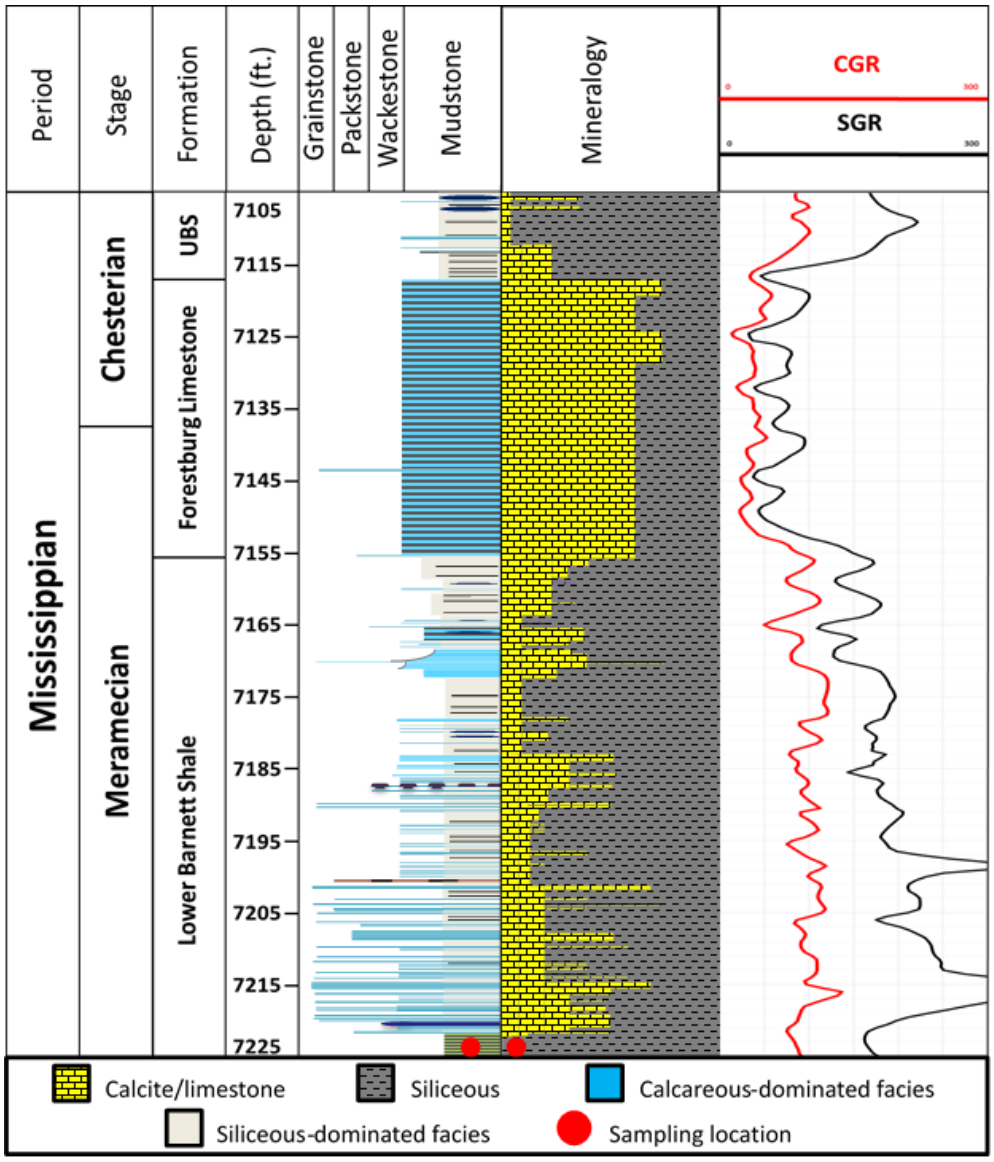

Figure 2. Combination stratigraphy column, lithofacies, and spectral and cumulative gamma ray logs for Blakely #1 core. Our core plugs (red circle) are from siliceous mudstone section. (Period and stage from Jarvie et al., 2007; mineralogy and grain size from Loucks and Ruppel, 2007; SGR and CGR logs from Rotary Laboratories, Midland, Tex.). UBS = Upper Barnett Formation; SGR = spectrum gamma ray; CGR = cumulative gamma ray. Texture classification (Grainstone, Packstone, Wackestone, Mudstone from Dunham (1962).

Intensive XRF scanning of the Blakely #1 core by Rowe et al. (2008) observed five distinct lithofacies: (1) Upper Barnett Formation member–laminated siliceous, organic-rich mudstone; (2) Forestburg limestone member–laminated argillaceous, lime mudstone; (3) Lower Barnett Formation member 1–laminated argillaceous, organic-rich mudstone; (4) Lower Barnett Formation member 2–laminated siliceous, organic-rich mudstone; and (5) Lower Barnett Formation member 3–laminated ferroan dolomite–rich, organic-rich mudstone (Figure 3).

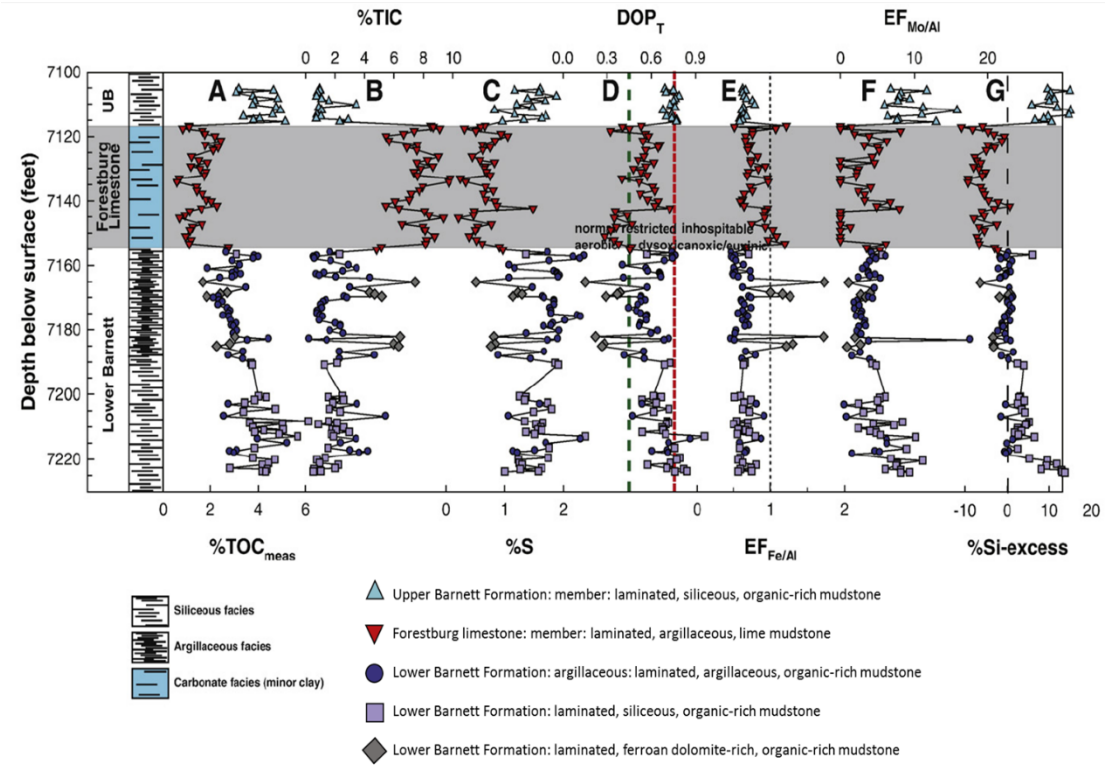

Figure 3. High-detail XRF-scanning results from Texas United Blakely #1 core, from Rowe et al. (2008), showing fluctuation of various geochemical factors along with vertical variation between five distinct lithofacies.

An organic-matter content analysis (Loucks and Ruppel, 2007) for the Blakely #1 suggests a varying amount of organic material that correlates with the observed lithofacies (Figure 3) (Rowe et al., 2008) and the gamma-ray-log profiles (Figure 2). The upper Lower Barnett Formation portion of the Blakely #1 retains the highest average amount of organic material at 4.0 wt % TOC, which agrees with the range of TOC observed for the Lower Barnett Formation member 2 lithofacies (2.9–6.0 wt % TOC) (Loucks and Ruppel, 2007; Rowe et al., 2008). The TOC content for Lower Barnett Formation members 1 and 3 is high, ranging from 1.9 to 5.5 wt % TOC (Loucks and Ruppel, 2007; Rowe et al., 2008). The TOC value for the Upper Barnett Formation member ranges from 3.0 to 5.6 wt %, and the Forestburg limestone average TOC value of 1.8 wt % is well within the range of TOC observed for the Forestburg limestone (0.6–2.7 wt % TOC) (Loucks and Ruppel, 2007; Rowe et al., 2008).

Chapter 3: Samples and Methods

SAMPLES AND SAMPLE PREPARATIONS

Core-plug samples collected for this study are within a constrained stratigraphic interval in the upper part of the Lower Barnett Formation siliceous mudstone interval, from the Texas United Blakely #1 well core, Wise County, Texas. The organic-rich interval (TOC = 6.6 wt %) of the Lower Barnett Formation at 7,222 ft below ground surface was chosen for its high maturity (Ro = 2.01%) to limit the effect of liquid hydrocarbons on adsorbed gas measurements (Zhang et al., 2012). The dominant lithofacies at the 7,222-ft depth interval is described as a laminated, siliceous, organic-rich mudstone (Loucks et al., 2007; Rowe et al., 2008).

Seven 3/8-inch outer diameter (OD) core plugs, along with one 1-inch OD core plug, were drilled from within a vertically constrained 2-inch interval located within the 7,222-ft section in an attempt to account for the effect of depth on sample heterogeneity (Figure 4). The samples were plugged parallel to bedding using custom 6-3/4-inch long diamond-impregnated Scorpion Engineering, Inc., core-sampling bits (1/16-inch kerf, #33 Jacob's Taper), in either 3/8-inch or 1-inch inner diameter (ID) on a water-cooled JET Tools J-A5816 drill press at the Austin Core Research Center of the Bureau of Economic Geology (Bureau). The single 1-inch OD core plug and the 3/8-inch OD core plugs were sampled to be preserved for future work.

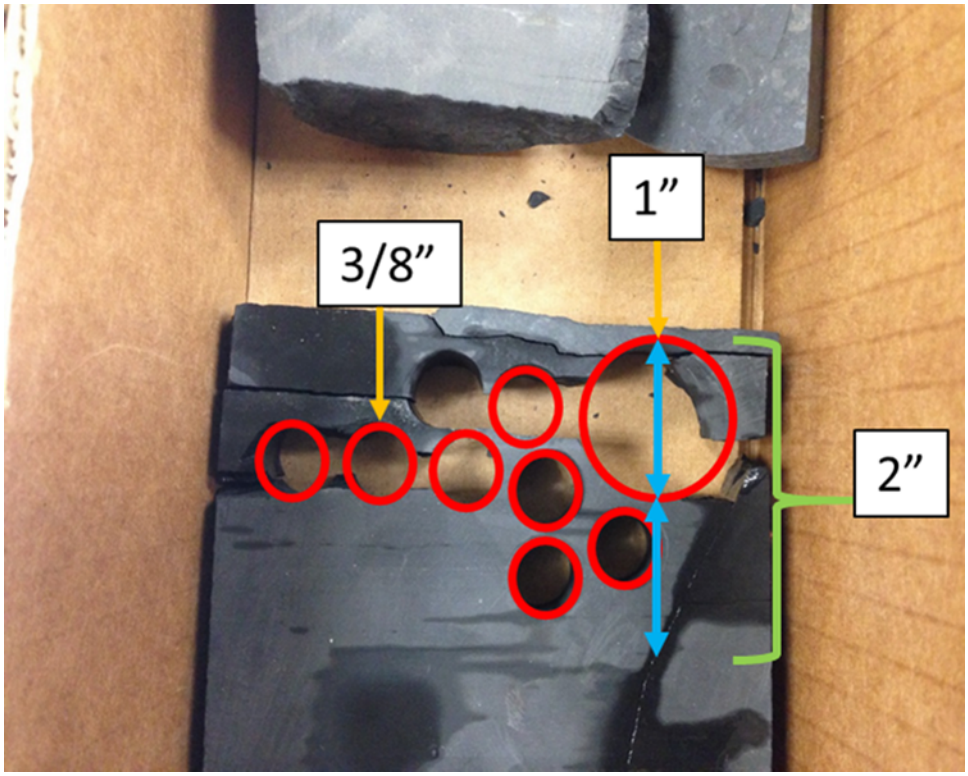

Figure 4. 2-inch vertical sampling interval located at approximately 7,222-ft depth interval below ground surface, showing plugging locations of all 3/8-inch (small red circles) and single 1-inch OD (large red circle) core plugs used in this study.

The two sets of core plugs were then dried in a fume hood for 24 h at room temperature in the Bureau’s Gas Geochemistry Laboratory. The weight of the single 1-inch OD core plug and 3/8-inch OD core plugs was measured using a Denver Instrument P-124 Pinnacle Series precision analytical balance with 0.01 mg accuracy. Each individual 3/8-inch core plug was then cut, sanded, and weighed incrementally to accurately normalize its individual weight to one-seventh of the weight of the 1-inch core plug to ensure that the combined masses of the seven 3/8-inch core plugs and the 1-inch

core plug were nearly identical (Table 1). The 3/8-inch plugs were then hand cut and sanded to a length perpendicular to the plug's long axis (perpendicular to bedding) with a Dremel Model 3000 rotary tool using 420 grit 1/2-inch sanding drums. The lengths and diameters of the 1-inch and 3/8-inch core plugs were then measured three times each using a set of Mitutoyo CD-8-inch ASX Digimatic calipers with 0.01-mm accuracy, to establish average dimensions along with 2-sigma standard deviation of measurement.

Table 1

Measured dimensions of 7 total 3/8-inch and one 1-inch OD core-plug samples

Depth (ft)	Sample	Length (mm)	Diameter (mm)	Volume (mL)	Initial Weight (g)
7222	1"	17.42	25.37	8.81	21.8161
	3/8" Total	18.52 ± 0.89	9.25 ± 0.08	8.70	21.8145

The 3/8-inch core plugs were then placed together into a Lindberg/Blue M VO914C vacuum oven for dewatering, until sample weight stabilization, over a total of 72 h. Dewatering was performed at 130°C in an effort to limit the effect of inherent and sampling-derived moisture on clay minerals and adsorption sites that could result from using a temperature higher than the minimum temperature (110°C) shown to remove free-pore water via the retort method (Handwerger et al., 2012). The masses of each 3/8-inch core plug were measured every 24 h to quantify the change in mass owing to water loss from the samples and to determine the ultimate dewatered sample mass (Table 2). The samples were immediately transferred into a jar containing 20–40 mesh (0.841–

0.420 mm) anhydrous calcium sulfate (CaSO4) desiccant upon removal from the oven. Samples not being handled during measurements were confined to the desiccant jar to minimize the adsorption of atmospheric moisture on the samples.

Table 2

Mass measurements for seven 3/8-inch and one 1-inch OD core plugs for dewatering at 130°C

Mass Difference Stability #	Time (h)	Measured 1" Plug Weight (g)	Measured 3/8" Total Weight (g)
1	0	21.816	21.815
2	24.117	21.743	21.738
3	48.067	21.741	21.738
4	71.583	21.737	21.733

GRI (CRUSHED SHALE) ANALYSIS HELIUM PYCNOMETRY

Several rock chips from along the same 2-inch wide interval sampled for the seven 3/8-inch and single 1-inch core plugs were taken and ground into a 20–30 mesh (595–843 μm) powder using a ceramic mortar and pestle. Thirty g of the 20–30 mesh-sized powder was dewatered at 130°C for 72 h in the Lindberg/Blue M vacuum oven before undergoing Boyle's Law helium porosimetry in the Bureau's Porosity, Permeability, and Pore-Scale Processes Laboratory (P3 Lab). The porosimetry methodology of the P3 Lab is a modified gas-expansion procedure developed by Cui and Bustin (2010) that is based on the accepted industry-standard Gas Research Institute

(GRI) technique (Carslaw and Jaeger, 1959; Cui et al., 2009; Cui and Bustin, 2010; Peng and Loucks, 2016).

EXPERIMENTAL SETUP FOR GAS ADSORPTION

The custom-built volumetric adsorption instrument located at the Bureau's Gas Geochemistry Laboratory (Figure 5) was also used for this study (Zhang et al., 2012). The experimental setup consists of a gas source and/or vacuum pump connected to an HP5890 gas chromatograph (GC) oven containing a coupled reference cell of known volume (2.16 mL) for gas storage and a sample cell presented via simplified cartoon in **Figure 6**.

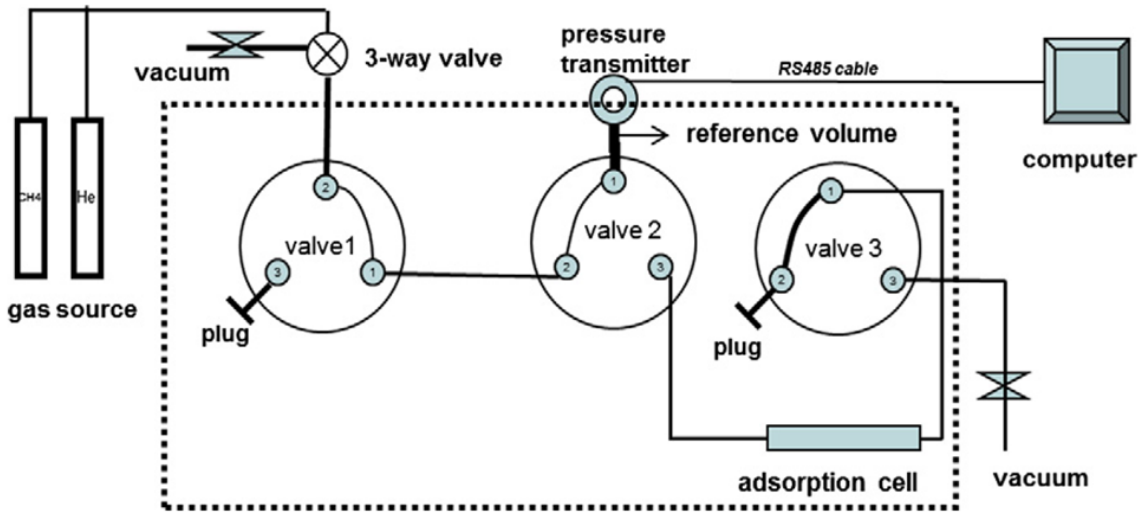

Figure 5. Experimental setup schematic for methane isotherm measurements (from Zhang et al., 2012).

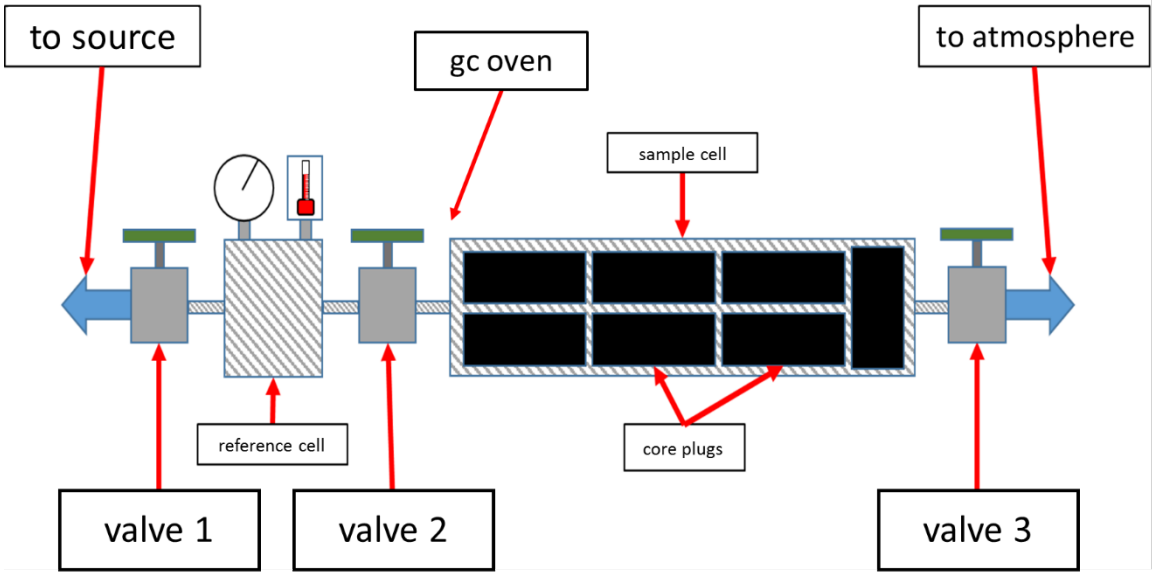

Figure 6. Simplified experimental-setup schematic showing reference cell with pressure transducer and thermocouple, sample cell filled with core-plug samples, and three pneumatic valves contained within gas chromatograph oven.

The gas source—a tank of Praxair HE 5.0UH-6K ultra-high purity grade (99.999%) compressed helium at 6000 psig or Praxair ME 3.7UH-K ultra-high purity grade (99.97%) compressed methane at 2500 psig—is connected to the instrument, along with an Edwards XDS-10 dry-scroll vacuum pump, by 1/4-inch Swagelok tubing and a series of Swagelok SS-42GXS4 three-way valves and Swagelok SS-42GS4 two-way valves. Within the GC oven portion of the instrument sits a network of three VICI Instruments Co., Inc., Valco A90 pneumatic two-position valve actuators and Swagelok 1/16-inch tubing connecting the coupled reference cell and sample cell to the gas source and vacuum pump. The three pneumatic valves are computer controlled by a Wasson-ECE Automator (Ver. 4.3.0) bench-top controller, and the temperature and pressure are computer monitored and recorded using Keller-America READ30 (Ver. 2.6) software.

The custom-built reference cell is connected to the first port of the second pneumatic valve along with a Keller–Druckmessternik Type PA-33X/80801/5000PSIS high-precision (0.01% FS) pressure transducer and thermocouple. The sample cell was built using a combination of off-the-shelf Swagelok components, specifically a single SS-1610-61BT bore-through bulkhead union, two SS-1611-PC-4 1-inch x 1/4-inch tube OD reducing port connectors, two SS-400-6-1 1/4-inch x 1/16-inch tube reducing unions, two NI-8-VCR-2-GR-2M nickel-plated sintered inline filters that prevent particles from entering the pneumatic valves, and a single Applied Porous Technologies, Inc., 0.988-inch x 0.500-inch x 2-µm 316L stainless-steel sintered cylinder used to reduce dead volume (**Figure 7**).

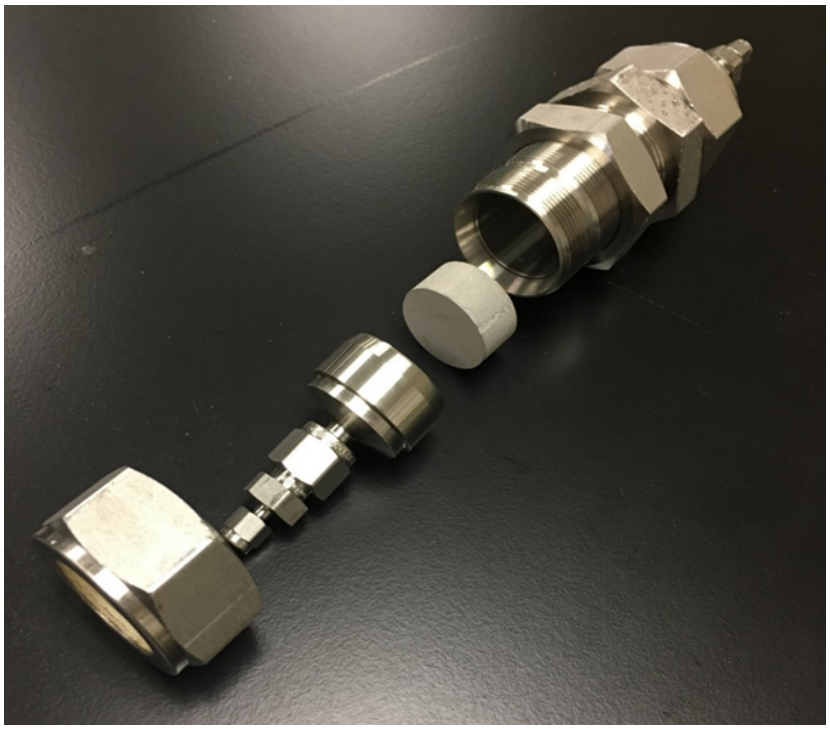

Figure 7. Photograph of sample cell used in this study.

System-leak tests were performed periodically throughout this study, in accordance with Zhang et al. (2012), to quantify the leakage of gas expected from the system during experimental procedures. System-leak tests were performed after connecting the sample cell to the system and prior to sample cell-void-volume measurements, adsorption measurements, and lost-gas measurements. The 3/8-inch core-plug samples were quickly transferred into the sample cell from the desiccant jar and then sealed. The leak test commenced by quickly placing the sample cell into the GC oven and connecting it with the system between port 3 of the second valve and port 1 of the third valve. The system-leak tests were conducted at constant temperature of 35.4°C and performed by connecting the reference cell and sample cell together via pneumatic valve 2, then incrementally pressuring the system with helium to 15MPa (2175.57psi) and monitoring the pressure drop for up to 24 h. Individual system-leakage tests were terminated once an accepted leakage rate of 6.89×10^{-4} MPa/h was attained (Zhang et al., 2012).

The void volume of the sample cell was determined through a series of gas-expansion tests using pressurized helium, performed under isothermal conditions at 35.4°C. Because helium is considered to be inert and nonsorbing, it is used to perform these volumetric measurements (Lu et al., 1995; Krooss et al., 2002; Goodman et al., 2004; Keller and Staudt, 2005; Zhang et al., 2012). The measurement of the reference-cell volume and sample-cell volume was performed with and without a laboratory-standard nickel cylinder of known density and mass (8.91 g/cm^3, 3.4037 g) being present within the sample cell (Zhang et al., 2012). In view of these conditions, "sample-cell

void volume" refers to the space within the sample cell not physically occupied by the solid 3/8-inch core-plug samples, and "system volume" refers to the sum of the sample-cell void volume and reference-cell volume. After the leak test, the sample and reference cells remained connected and were then vacuumed for ~15 min and the pressure recorded. The sample cell was isolated, and helium was charged into the reference cell and the pressure recorded. Pneumatic valve 2 was then turned, allowing the helium to charge into the sample cell, with the pressure recorded once equilibrium was reached. The reference-cell pressure was increased to an assigned pressure condition that allowed for additional helium gas to charge into our samples. The procedure of gas filling into the reference cell and gas charging into the sample cell was repeated eight to ten times at subsequently higher pressure level.

CH_4 ADSORPTION ISOTHERM MEASUREMENTS

A methane isotherm measurement was performed under isothermal conditions at 35.4°C in accordance with the adsorption isotherm methodology presented in Zhang et al. (2012). The methane isotherm is measured to determine the relationship between the amount of gas adsorbed onto the surface area of the sample pore volume and gas pressure under isothermal conditions. After the sample-cell void volume measurement was completed, the system was vacuumed for 2 h to get rid of helium. A certain amount of methane was then charged into the reference cell and allowed to equilibrate. The pressure was monitored until a pressure change of 6.89×10^{-4} MPa was achieved over a 5-min timespan. The valve between the reference and sample cell, pneumatic valve 2, was then turned, allowing the gas to expand into the sample cell. The gas was allowed to

equilibrate over the course of 24 h per pressure point because of the use of the 3/8-inch outer-diameter core plugs as samples. Equilibration of these samples, compared to that of powdered samples typically used in adsorption measurements, required a much longer equilibration time as a result. The procedure of gas filling into the reference cell and gas charging into the sample cell was repeated 20 times at different gas-pressure levels ranging from 100 psig to 1800 psig.

CH_4 GAS RE-SATURATION, EXPOSURE, AND DEGASSING

CH_4 gas resaturation, exposure, and degassing measurements were performed on 3/8-inch core-plug samples at an isothermal temperature of 35.4°C, using the same experimental setup (**Figure 6**, **Figure 8)**. The gas-resaturation portion of the experimental method is modified from the "batch pressure decay" method, in which, under isothermal conditions, gas is reintroduced into a sample at high pressure before the pressure is allowed to decay and equilibrate over time (Riazi, 1996; Haugen and Firoozabadi, 2009; Etminan et al., 2010, 2012, 2013). The degassing-measurement segment is akin to the "canister gas evolution" or "canister desorption" presented in numerous lost-gas publications, wherein degassing data is acquired after placing a sample within an isothermal airtight canister and the increase in pressure within the canister is monitored over time (Bertard et al., 1970; Kissell et al., 1973; Shtepani et al., 2010; Seidle, 2011; Hosseini et al., 2015). The exposure phase of the experiment is performed to attempt to simulate the reduction in pressure experienced by shale-gas canister core samples in the field during the coring process and their ensuing trip upward within the borehole while surrounded by drilling mud (Seidle, 2011).

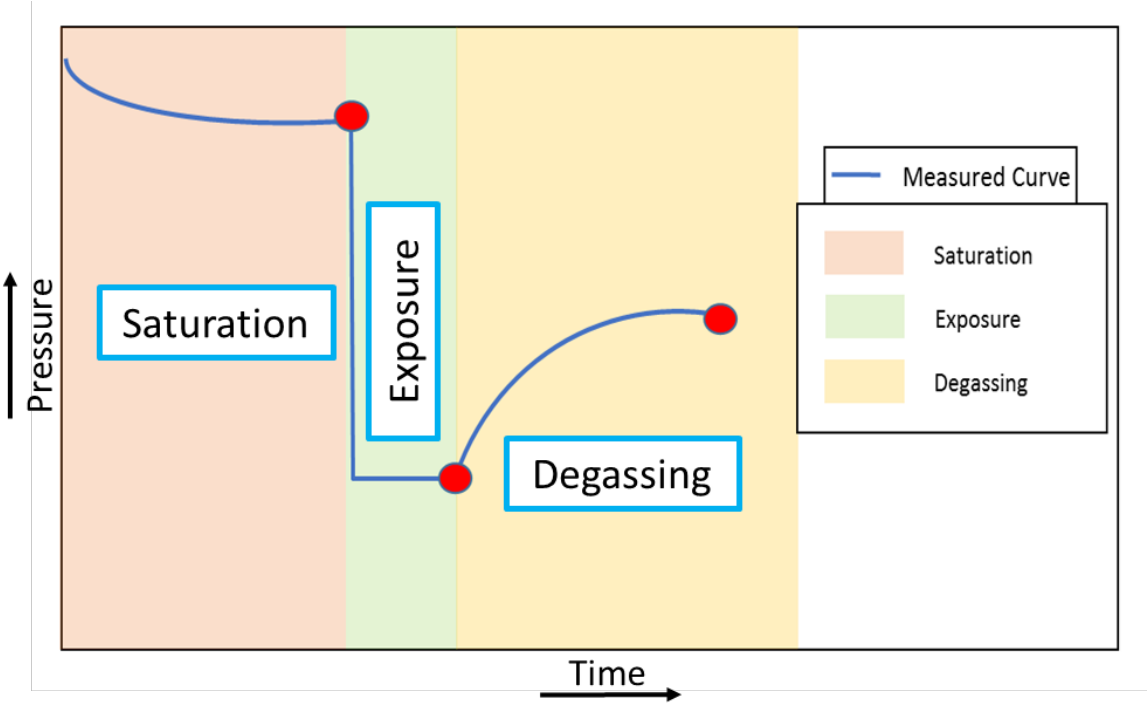

Figure 8. Simplified view of the three experimental phases: saturation, exposure, and degassing.

Gas resaturation commences with CH_4 being charged into the reference cell before connecting the sample cell and reference cells together for the same amount of time. This process is performed repeatedly by rapidly turning pneumatic valve 2, which allows the gas from the reference cell to expand into the sample cell at progressively greater pressures. The combined charging and expanding process stops once a predetermined pressure (saturation pressure) is reached within the system volume. Pneumatic valve 1 is then closed, disconnecting the gas source from the sample volume. The CH_4 within the sample volume is then allowed to equilibrate over time into the samples until a decay rate of approximately 0.1 psi/h (6.89×10^{-4} MPa/h) is attained, typically ~24 h. The experiment then proceeds into the exposure phase, in which the

system volume is opened to atmospheric conditions at 35.4°C. The isolated system volume is exposed to atmosphere by the opening of pneumatic valve 3, which causes the CH_4 surrounding the samples within the system volume to be vented. The resulting drop in pressure, under isothermal conditions, is monitored and timed to start and stop after a predetermined allotment of time dependent on the type of experiment being run. Once the specific exposure time is reached, pneumatic valve 3 is turned on, resulting in the reisolation of the system volume. The degassing phase of the experiment is immediately entered with the closing of pneumatic valve 3. The pressure build up within the system volume is monitored and recorded.

Saturation pressure and exposure time were hypothesized to be two possible controlling experimental parameters that affect lost gas, and so two different sets of experiments (resaturation + exposure + degassing) were performed to quantify their potential effects on lost-gas values. The first set of experiments varied the initial saturation pressures from 177, 517, and 1072 psia to 1699 psia, at 35.4°C and a fixed exposure time of 4 min. The second set of experiments varied the exposure time from 0.53, 8, and 32 min to 136 min, at 35.4°C and a fixed initial-saturation pressure of 1781.53 psia.

Chapter 4: Data and Results

CH_4 ADSORPTION ISOTHERM OF 3/8-INCH CORE PLUGS AT 35.4°C

The measured sorption isotherm on 3/8-inch core plugs is an important part of determining adsorbed gas, under experimental temperature conditions (35.4°C), at CH_4-resaturation pressure and the peak of degassing (**Figure 9**). The method for determining the quantity of adsorbed methane, per experimental pressure level, is taken from the work of Lu et al. (1995) and presented in Zhang et al. (2012). Pressure conditions during the methane-adsorption isotherm measurement were recorded before and after the methane was allowed to expand into the sample cell from the reference cell. The NIST thermophysical-properties database, on the basis of equations of state from McCarty and Arp (1990) and Setzmann et al. (1991), was used to determine the density of methane at each pressure condition at 35.4°C. The resulting calculated gas molar densities at these two pressure stages were used to quantify the amount of gas adsorbed per pressure level.

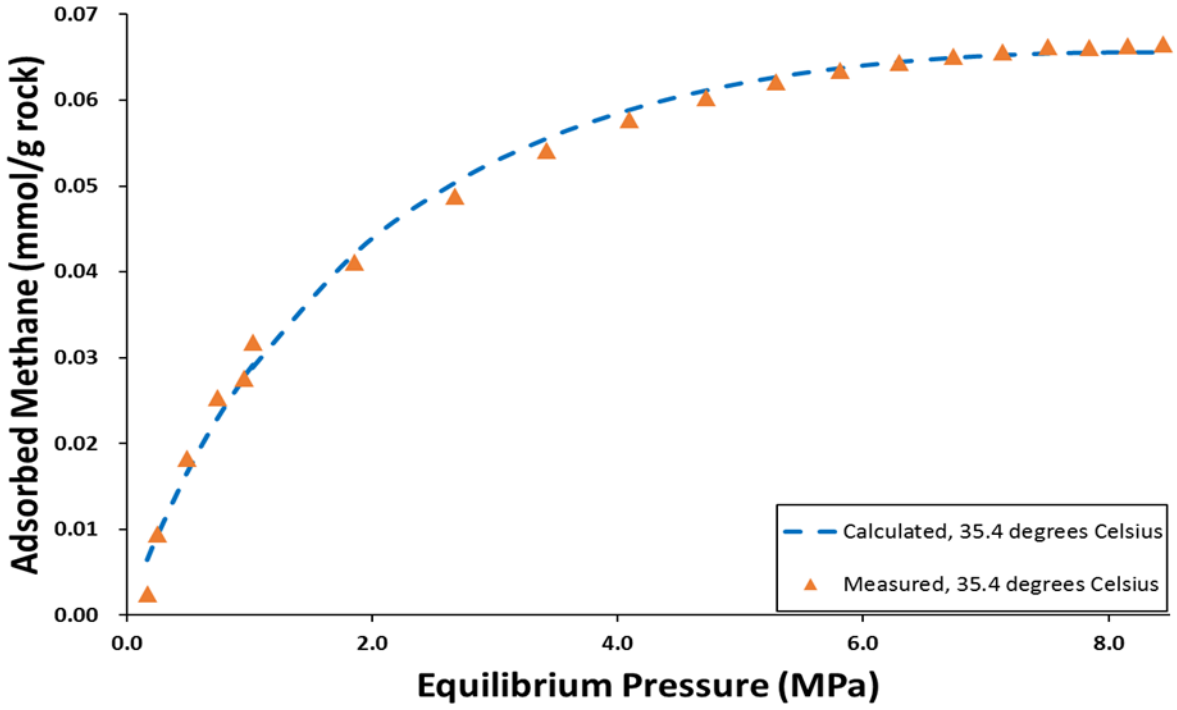

Figure 9. Measured (triangles) and calculated (blue dashed line) methane-adsorption isotherm at 35.4°C.

Equation 1 is used for determining the amount of excess sorbed gas, Nads (P), at a given pressure condition according to Lu et al. (1995) and Zhang et al. (2012).

$$N_{ads}(P) = N_{total}(P) - N_{ref}(P) - N_{void}(P) \quad \text{..... (Equation 1)}$$

In **Equation** 1, P in MPa is the system equilibrium pressure condition. The total amount of gas charged into the system volume over the entire adsorption isotherm experiment up to pressure P is N_{total} (P), in mmol. The amount of gas that remains in the reference volume at each respective equilibrium condition is N_{ref} (P), in mmol; the amount of gas that can charged into the sample-cell void volume is N_{void} (P), in mmol.

Equation 2, from Lu et al. (1995), can be reformulated to calculate the amount of excess sorbed gas based on molar gas densities at the "ith" iteration.

$$N_{ads}(i) = V_{ref}\sum_{j=1}^{i}[\rho_c(j) - \rho_e(j)] - V_{void} * \rho_e(i) \;\; i = 1, 2, \ldots n \quad \text{..... (Equation 2)}$$

In **Equation 2**, the amount of excess sorbed gas can be calculated according to molar gas densities at the "ith" iteration. N_{ads} (i) = amount of excess sorbed gas (mmol); V_{ref} = reference-cell volume (mL); V_{void} = sample-cell void volume (mL); ρ_c = density of methane in V_{ref} prior to gas expansion (mmol/mL); and ρ_e = density of methane within (Vref + Vvoid) at equilibrium (mmol/mL). The isotherm was created by repeating the experiment until the highest desired equilibrium gas pressure point of 8.44 Mpa was reached (Figure 9). It was hypothesized that the measured methane isotherm could be described by the monolayer adsorption theory that depicts adsorbed gas molecules forming a single coherent layer on various adsorption sites of comparable energy (Langmuir, 1918; Gregg and Sing, 1982; Keller and Staudt, 2005; Zhang et al., 2012).

The model we used to calculate the amount of gas adsorbed onto pore surfaces with gas pressure under isothermal conditions was the modified Langmuir equation (**Equation 3**).

$$Q = Q_{max} * \frac{k*P}{1+(k*P)} * \left(1 - \frac{\rho_f}{\rho_a}\right) \quad \text{.....(Equation 3)}$$

In **Equation 3**, Q = excess adsorbed gas (mmol/g rock); Q_{max} = Langmuir maximum (mmol/g rock); k = Langmuir constant (1/Mpa); P = pressure (Mpa); ρ_f = free gas density (mmol/mL); and ρ_a = adsorbed phase density (mmol/mL). The modified Langmuir

equation is similar to the Langmuir equation presented in Zhang et al. (2012); however, the former accounts for the significant density difference between the sorbed- and free-gas phases by utilizing each respective value in the calculation of excess gas adsorption (Sircar, 1999; Do and Do, 2003; Gensterblum et al., 2009, 2010; Gasparik et al., 2012, 2013; Hu et al., 2015).

A least-squares regression analysis was used to fit the calculated adsorbed gas based on the modified Langmuir equation to the measured methane adsorption isotherm (Figure 9); the fitting follows the procedure described in Zhang et al. (2012). The Langmuir maximum (0.1059 mmol/g rock), Langmuir constant (0.3788 1/Mpa), and density of the adsorbed phase (19.85 mmol/mL) are obtained through the least-squares fitting methodology. Experimental measured and calculated adsorbed methane values are listed in **Table 3**.

Table 3

Measured and calculated adsorbed methane values at 35.4°C

Pressure Stage	Equilibrium Pressure (MPa)	Free-Gas Density ($mmol/cm^3$)	Adsorbed Methane (mmol/g rock)	
			Measured	Calculated
1	0.17	0.07	0.002	0.006
2	0.25	0.10	0.009	0.009
3	0.50	0.19	0.018	0.017
4	0.74	0.29	0.025	0.023
5	1.03	0.41	0.032	0.029
6	0.96	0.38	0.028	0.028
7	1.86	0.74	0.041	0.042
8	2.67	1.09	0.049	0.050
9	3.42	1.40	0.054	0.056
10	4.10	1.70	0.058	0.059
11	4.72	1.97	0.060	0.061
12	5.29	2.23	0.062	0.063
13	5.81	2.47	0.063	0.064
14	6.29	2.69	0.064	0.065
15	6.73	2.90	0.065	0.065
16	7.13	3.08	0.066	0.065
17	7.50	3.26	0.066	0.065
18	7.84	3.42	0.066	0.066
19	8.15	3.57	0.066	0.066
20	8.44	3.71	0.067	0.066

DEGASSING CURVES OF VARIABLE SATURATION PRESSURES AND EXPOSURE TIMES

The two distinct sets of degassing curves produced from the experiments that either vary the amount of gas initially charged into the samples or vary the amount of time during which the samples were exposed to atmospheric conditions. Degassing curves from the first set of four experiments involved altering of saturation pressures, and fixing the exposure time (Figure 10). Four experiments were performed at 35.4°C; each

individual curve, in ascending order, represents the saturation pressure of the samples from 177, 517, 1072, and 1699 psia. Exposure time periods for this set of experiments were fixed at 4 min. The gas release rate is extremely high, with more than 60% of the total charged gas released in the first 20 min of degassing time, regardless of large variations in initial gas-saturation pressure (**Figure 10**). The cumulative gas volume shown in the degassing curve increases with each subsequently elevated saturation pressure (**Figure 10**).

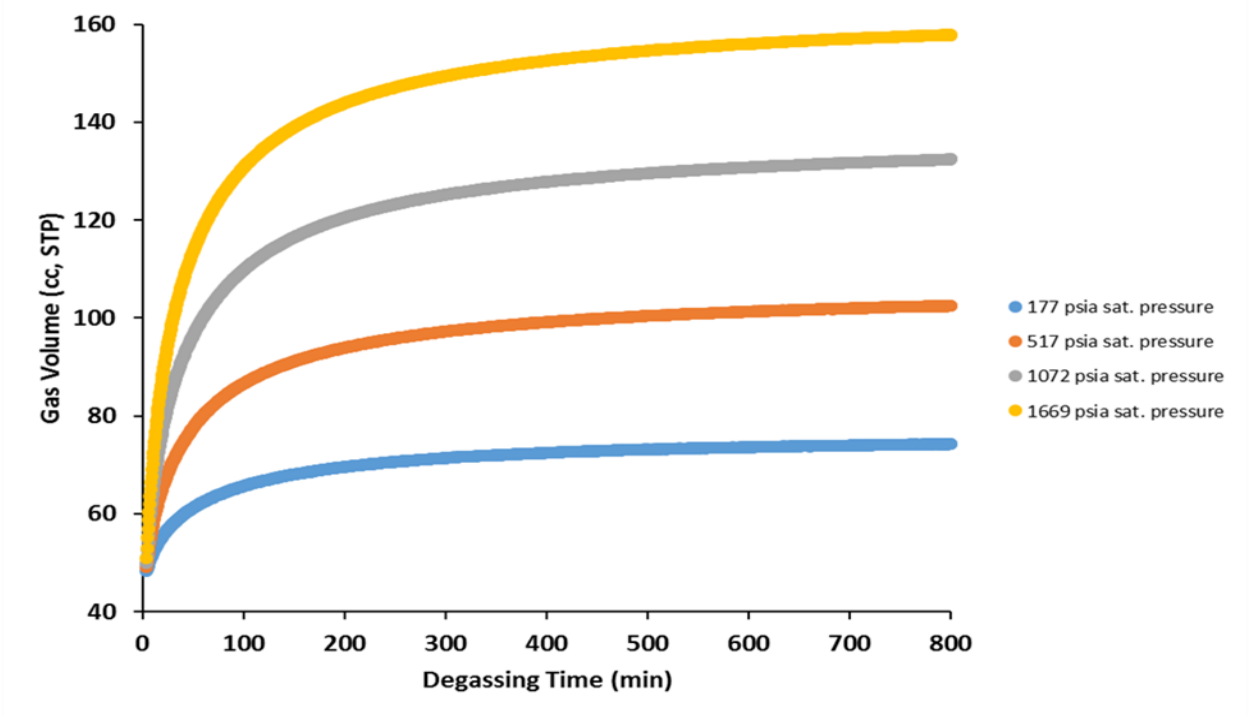

Figure 10. Experimentally measured degassing curves at varying CH4 saturation pressure and constant exposure time of 4 min at 35.4°C.

Degassing curves were produced through a second set of experiments that altered exposure times and fixed saturation pressure (**Figure 11**). These four experiments were

performed at 35.4°C, with saturation pressure fixed at 1781.54 psia while varying exposure times from 0.53, 8, 32, and 136 min, respectively. The released gas volumes of the degassing curves from CH_4-saturated core plugs increase at significantly higher rates at a 0.53-min exposure time compared to those at longer exposure times. Released gas volumes of the initial portions of the degassing curves are observed to increase linearly at significantly higher rates compared to the latter portions of the curve that increase nonlinearly at a reduced rate. Cumulative gas volumes appear to dramatically decrease from curve to curve with increasing exposure time (**Figure 11**).

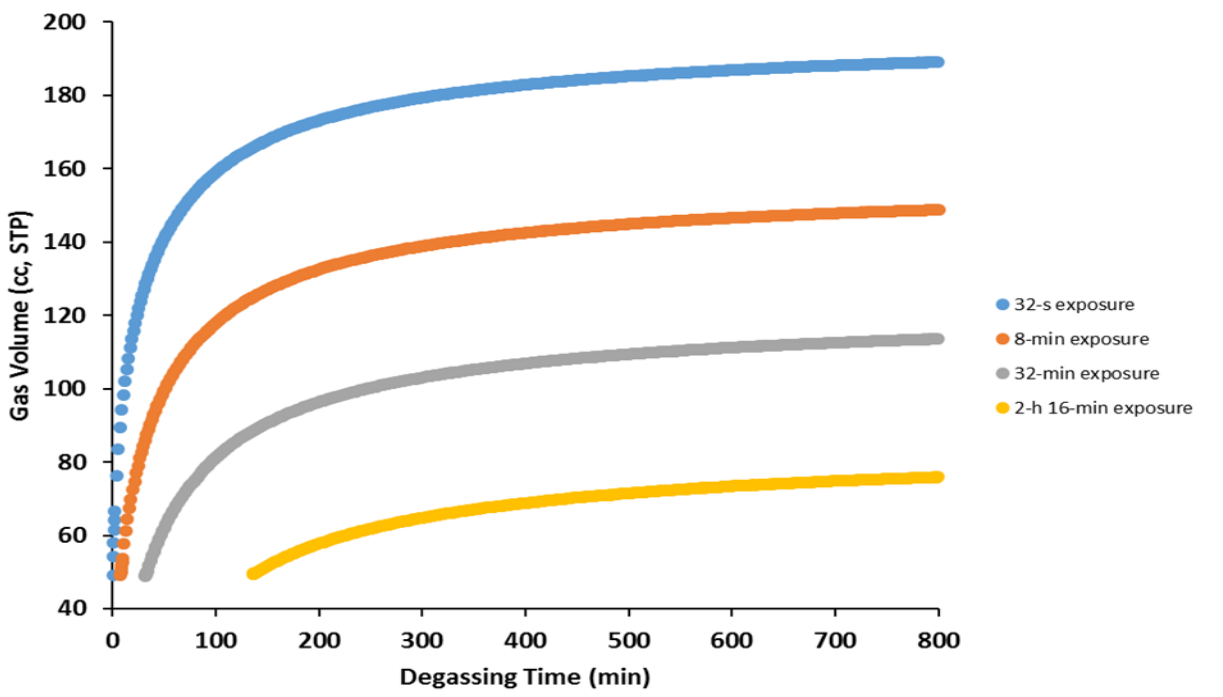

Figure 11. Experimentally measured degassing curves at varying exposure times and fixed CH_4 saturation pressure of 1781.5 psia at 35.4°C.

MASS-BALANCED APPROACH TO DETERMINE AMOUNT OF LOST GAS

The mass balance of the three-phase experimental procedure allows for a quantitative assessment of the volume of gas lost from the samples during the period of exposure to atmospheric conditions. Three different and distinct experimental reference points are assigned for the mass-balance evaluation of lost gas: saturation-equilibrium, initial-degassing, and peak-degassing conditions (**Figure 12**). The saturation-equilibrium reference point corresponds to the pressure at which the primary amount of gas is charged into the samples. The initial-degassing reference point indicates the pressure and time when gas was initially emitted from the samples and peak-degassing reference points indicate the pressure and time at which the greatest amount of gas emitted from the samples.

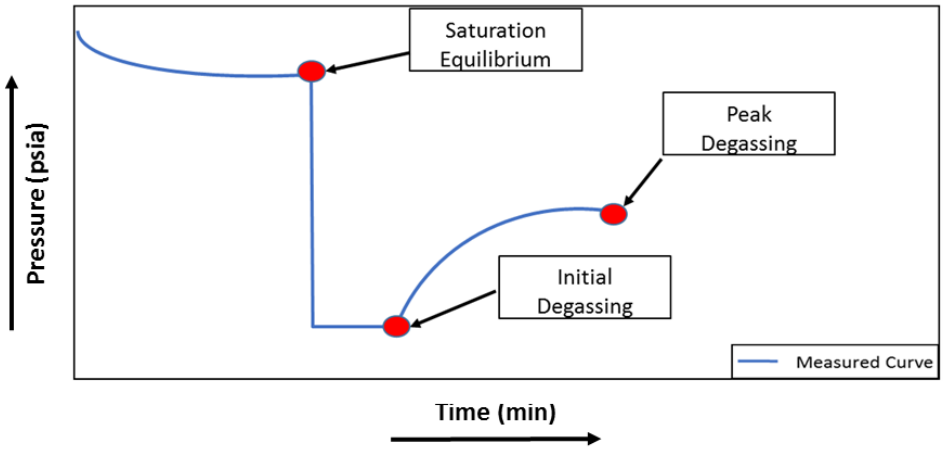

Figure 12. Three different mass-balance calculation reference points in red representing pressure of saturation equilibrium, initial degassing, and peak degassing.

Calculating lost gas involves knowing the mass of gas initially charged into the samples at saturation (**Equation 4**), the mass of gas emitted from the samples between

initial and peak degassing (**Equation 5**), and the mass of gas retained in the samples at the peak of the degassing curve (**Equation 6**).

$$M_{\text{Gas Charged In}} = M_{\text{Free,Saturation}} + M_{\text{Adsorbed,Saturation}} \quad \text{(Equation 4)}$$

In **Equation 4**, $M_{\text{Gas Charged In}}$ = total gas charged into the samples (mmol), $M_{\text{Free,Saturation}}$ = amount of free gas in pore volume (mmol), and $M_{\text{Adsorbed,Saturation}}$ = amount of sorbed gas on pore surface area (mmol).

$$M_{\text{Emitted,CorePlug}} = M_{\text{System,Peak}} - M_{\text{System,Initail}} \quad \text{(Equation 5)}$$

In **Equation 5**, $M_{\text{Emitted,Core Plug}}$ = total gas emitted from core plugs (mmol),$M_{\text{System,Peak}}$ = amount of free gas in system volume at peak degassing conditions (mmol), and $M_{\text{System,Initial}}$ = amount of free gas in system volume at initial degassing conditions (mmol).

$$M_{\text{Retained,Core Plug}} = M_{\text{Effective Free Gas,Peak}} + M_{\text{Adsorbed,Peak}} \quad \text{(Equation 6)}$$

In **Equation** 6, $M_{\text{Retained,Core Plug}}$ = total gas retained within core plugs (mmol), $M_{\text{Effective Free Gas,Peak}}$ = amount of free gas in pore volume at peak degassing conditions (mmol), and $M_{\text{Adsorbed,Peak}}$ = amount of adsorbed gas on pore volume surface area at peak degassing conditions (mmol).

To perform the mass-balance lost-gas calculation, input parameters (**Table 4**) such as the sample pore volume and system volume were measured through the performance of GRI helium porosimetry and helium void-volume measurements, respectively. Measured GRI porosity is 5.6%, and bulk density is 2.49 g/mL. Measured volumes were calculated for the sample-cell volume (39.82 mL), reference cell volume

(2.16 mL), sample-cell void volume (27.58), system volume (29.75 mL), 2-µm filter volume (3.61 mL), pore volume (0.49 mL), and measured sample volume (8.63 mL). The amount of gas that fills the system volume is considered to be composed solely of free gas, and the gas within the pore volume at each reference point is considered to be composed of free and sorbed gas.

Table 4

Input parameters for mass-balance calculation

Ref. Cell Volume (mL)	Sample-Cell Volume (mL)	Sample-Cell Void Volume (mL)	System Volume (mL)	2µm Filter Volume (mL)	Meas. Sample Volume (mL)	Pore Volume (mL)	Sample Bulk Density (g/mL)	Porosity (%)	Langmuir Maximum (mmol/g Rock)	Langmuir Constant (1/Mpa)	Adsorbed Phase Density (mmol/mL)
2.16	39.82	27.58	29.75	3.61	8.63	0.49	2.49	5.6	0.1059	0.3788	19.85

The mass-balance calculation for determining charged and retained gas in the samples at each reference point is shown in **Equation 7**:

$$M_{Total} = M_{Free\ Gas} + M_{Adsorbed\ Gas} \quad \text{(Equation 7)}$$

where M_{Total}= mass of gas in sample (mmol), $M_{Free\ Gas}$= mass of free gas charged into sample (mmol), and $M_{Adsorbed\ Gas}$= mass of gas adsorbed in sample (mmol). The amount of adsorbed gas at each reference point, in mmol, is calculated based on excess adsorbed gas shown in **Equation 3**, and the measured sample weight in grams is shown in **Equation 8**:

$$M_{Adsorbed\ Gas} = Q * W_{Sample} \quad \text{(Equation 8)}$$

where $M_{Adsorbed\ Gas}$= mass of gas adsorbed in sample (mmol), Q = excess adsorbed gas (mmol/g rock) calculated from **Equation 3**, W_{Sample}= measured weight of sample (g).

The adsorbed CH_4 phase of pure gases that attach to pore surfaces is considered to be significantly denser than the remaining free-gas phase within the pore volume (Sircar, 1999; Murata et al., 2001, Do and Do, 2003; Gensterblum et al., 2009, 2010; Gasparik et al., 2012, 2013; Hu et al., 2015). Binding energies between adsorbates (fluid) and adsorbents (solid) increase the potential for closer contact between CH_4 molecular and pore surfaces, thus forming a higher-density monolayer of adsorbed gas (Sircar, 1999; Do and Do, 2003). While a known theoretical adsorbed phase density is not currently available, it is presumed that adsorbed phase densities of methane approach but should not exceed the liquid phase density of methane (423 kg/m^3) (Do and Do, 2003; Gasparik et al., 2012). Our adsorbed phase density value, derived using the modified Langmuir equation for excess gas sorption (19.85 mmol/mL; 318.49 kg/m^3 at STP), does not exceed the liquid phase density of methane and agrees with a published range of adsorbed phase density values (200–600 kg/m^3) for organic-rich shales from the Netherlands (Gasparik et al., 2012).

Ambrose et al. (2010) present a preliminary correction for GIP estimations that accounts for the significant volume occupied by the high-density monolayer of adsorbed phase gases within pores. In routine GIP estimations, the volume of the free-gas phase is considered to be measured by a porosity measurement, which is then added along with the higher-density adsorbed volume measured by adsorption experiments (Ambrose et al.,

2010) but does not account for the significant density differences between the results of the free and adsorbed gas phase in GIP being erroneously overestimated. Ambrose et al. (2010) correct for this by characterizing the high-density adsorbed phase as restricting a portion of the pore volume available to the free-gas phase typically quantified by porosity measurements (**Figure 13**).

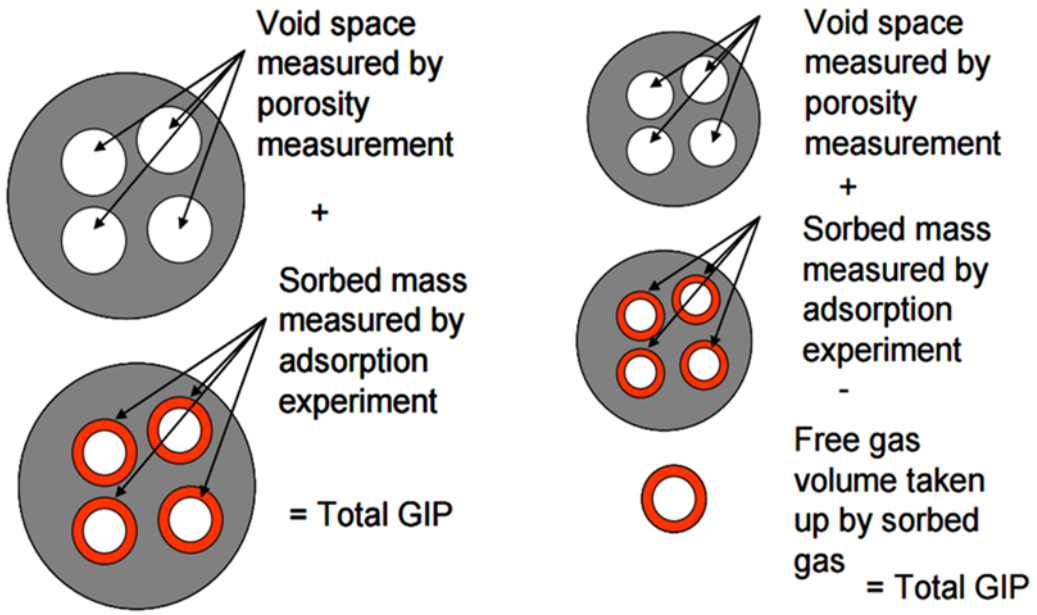

Figure 13. Schematic representing method for estimating free gas that doesn't account for volume of sorbed gas within pore volume (left), and method that corrects for volume of sorbed gas to quantify effective free gas (Ambrose et al., 2010).

The proper correction for pore volume available to the free-gas phase (effective pore volume) can be characterized as the difference between the pore volume typically quantified by porosity measurements and the volume occupied by the high density adsorbed gas phase (Ambrose et al., 2010). The amount of free gas within the system and

the sample effective pore volume, in mmol, is calculated based on gas molar density values (NIST thermophysical properties database) (**Equations 9** and **10**).

$$V_{\text{Eff. Free Gas}} = \left(V_{\text{Tot Pore Vol.}} - \left(M_{\text{Ads.}} * \frac{1}{\rho_a}\right)\right) \quad \text{(Equation 9)}$$

In **Equation 9**, $V_{Eff.\ Free\ Gas}$= effective free gas volume (mL), $V_{Tot\ Pore\ Vol.}$= total pore volume (mL), $M_{Ads.}$= mass of adsorbed gas (mmol), and ρ_a= adsorbed phase density (mmol/mL).

$$M_{\text{Eff. Free Gas}} = \rho_f * V_{\text{Eff. Free Gas}} \quad \text{(Equation 10)}$$

where $M_{Eff.\ Free\ Gas}$= free-gas mass in effective pore volume (mmol), $V_{Eff.\ Free\ Gas}$= effective pore volume for free-gas storage (mL), and ρ_f= free-gas density (mmol/mL). Effective pore volume for free-gas storage is the difference between total pore volume measured directly by helium porosimetry and the volume taken up by the measured adsorbed monolayer of methane (**Figure 13**) (Ambrose et al., 2010). Mass-balance-derived values for lost gas are determined by subtracting the sum of the gas emitted by the samples into the system volume and the gas retained within the core plug from the gas initially charged into the samples:

$$M_{\text{Lost}} = M_{\text{Gas Charged In}} - (M_{\text{Emitted,CorePlug}} + M_{\text{Retained,Core Plug}}) \quad \text{(Equation 11)}$$

where M_{Lost}= total gas lost from the samples during exposure time (mmol), $M_{Gas\ Charged\ In}$= total gas initially charged into samples (mmol), $M_{Emitted,\ Core\ Plug}$= total gas emitted from core plugs (mmol), and $M_{Retained,\ Core\ Plug}$= total gas retained

within core plugs (mmol). Mass-balance-calculated lost-gas values according to **Equation 11** are listed in **Table 5** for our two sets of experimental conditions.

Table 5

Mass-balance-derived lost-gas values from two sets of experiments

Conditions	Experiment (#)	Exposure Time (min)	Saturation Pressure (psia)	Mass-Balance-Derived Lost Gas (cc)
Varying Saturation Pressure	1	0.5	177	9.63
	2	0.5	517	22.65
	3	0.5	1073	37.17
	4	0.5	1699	54.65
Varying Exposure Time	5	0.53	1781.54	23.43
	6	8.03	1781.54	67.02
	7	32.02	1781.54	104.05
	8	136.05	1781.54	145.13

Chapter 5: Discussion

DEGASSING-MECHANISM ANALYSIS

Several publications that have analyzed the gas-releasing mechanism from CBM studies have previously plotted canister desorption (degassing) data versus the square root of time and have observed linear trends (Bertard et al., 1970; Kissell et al., 1973; Yee et al., 1993; McLennan et al., 1995; Diamond and Schatzel, 1998; Seidle, 2011). Gas desorption can be characterized as a diffusive process through Fick's law of diffusion by a partial differential solution for a spherical geometry taken from analogous examples involving heat flow (Crank, 1956; Carslaw and Jaeger, 1959; Mavor et al., 1990; Seidle, 2011). The partial differential equation for diffusion from a spherical geometry includes the square root of time, presented as either $\sqrt{t}$ or $t^{1/2}$ in the denominator, granting support to its linear relation to desorbed gas volume (Crank, 1956; Carslaw and Jaeger, 1959; Mavor et al., 1990). We hypothesize that if the measured degassing curves plotted versus the square root of time resulted in a linear trend, then the mechanisms could be mainly attributed to desorption.

The four degassing curves, where exposure time varies, were plotted versus the square root of time and are not feature a linear (**Figure 14a**). Onset portions of these degassing curves generally appear semi-elliptical in comparison to the more linear latter stage of degassing. The significant curvature examined from our measured degassing curves from organic-rich Barnett Formation core plugs suggests the mechanisms are more complicated and not directly related to gas desorption that dominantly occurs in CBM degassing.

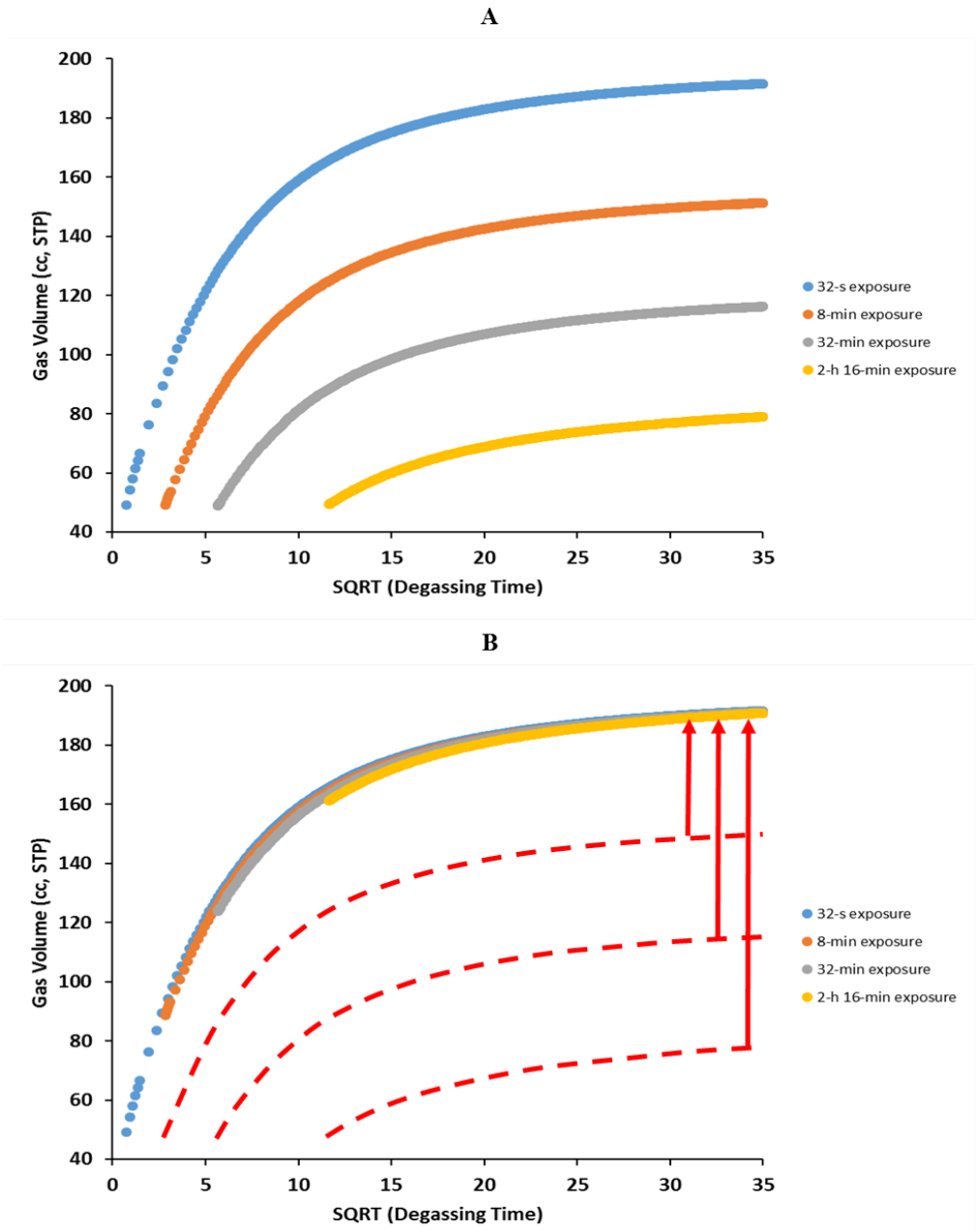

Figure 14. Experimentally measured degassing curves plotted vs. square root of degassing time at varying exposure times and 12.28 Mpa saturation pressure. (a) Measured degassing curves; (b) measured degassing curves overlapped with 32-s exposure curve after adding minimum amount of lost gas, as shown by red arrows.

Gas released from the organic-rich Barnett Formation could be a combination of two mechanisms: gas-volume expansion and gas desorption. We investigated the degassing curves attributed to the varying exposure-time experiments to better typify the timing of the different possible mechanisms that govern gas loss. The timing of the shift between the different mechanisms governing degassing can be characterized by assuming the 32-s exposure-time degassing curve experienced a negligible amount of gas loss. Thus, the difference in peak degassing volumes between the 32-s exposure-time curve and each longer exposure-time curve would be representative of the minimum amount of gas lost. We added this difference between peak degassing values to each respective degassing curve, resulting in the vertical translation of each curve. Once translated, all of the curves visibly overlap the 32-s exposure-time degassing curve at different degassing stages (**Figure 14b**).

This overlap reveals that each subsequent degassing curve represents a different stage of overall degassing as exposure time was incrementally increased. In addition, degassing phase-curve signatures noticeably shift from being visibly nonlinear to more linear as exposure time increases, suggesting that gas-releasing mechanisms change at different stages of degassing. Gas storage within shale-gas reservoirs can be classified into two distinct mechanisms: (1) gas compression and expansion ("free gas") within the pore volume, and (2) gas sorption ("sorbed gas") onto pore surfaces (Javadpour et al., 2007; Javadpour, 2009; Gasparik et al., 2013; Etminan et al., 2013; Hosseini et al., 2015). Gas expansion and gas desorption were considered the most representative degassing mechanisms on the basis of experimental timespan and observations from the curve

overlap. Gas can also be partially dissolved into organic matter by diffusion; Etminan et al. (2013) reported gas diffusion into organic matter requiring more than 50 h, which is nearly double our experiments' saturation phase of 24 h. Presumably, gas transported through organic matter by diffusion can be considered negligible under our experimental conditions. The curve overlap (**Figure 14b**) displays a distinct shift among the degassing curves between nonlinear and linear signatures with increasing exposure time. This suggests that despite both gas expansion and sorption being present throughout the overall degassing curve, gas expansion is more dominant at the beginning and decreases over time as gas desorption becomes more dominant (**Figure 15**).

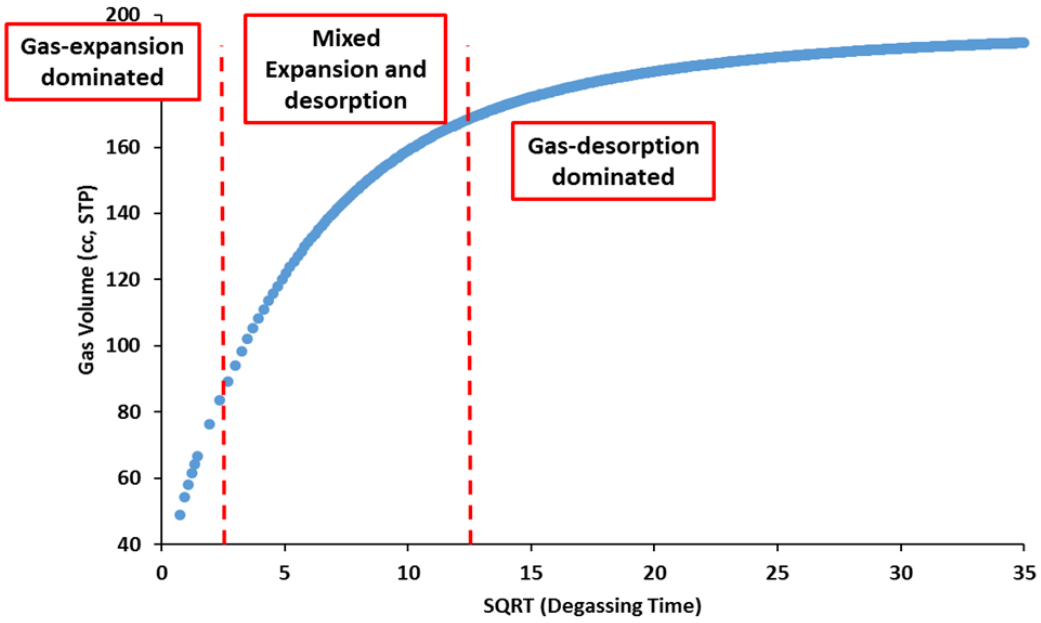

Figure 15. Overall degassing curve showing distinct zones of dominance by the two identified gas-loss mechanisms.

DOMINANT FACTORS AFFECTING LOST GAS

Lost-gas values determined by mass-balance calculations vary from 9.63 to 54.65 cc at standard temperature and pressure (STP), and linearly correlate with increasing saturation pressure (**Figure 16a**), suggesting that the effect of pressure on lost-gas estimation can be approximated based on a linear correlation for given set of rock properties. In contrast, mass-balance lost-gas volumes range from 23.24 cc at STP with 0.53 min of exposure time to 145.13 cc with 136 min of exposure time and nonlinearly relate to increasing exposure time (**Figure 16b**). When the amount of lost gas is normalized to that of initial gas charged into the samples and reported as a percentage, lost gas ranges from 23% to 31% of the charged gas with varying saturation pressure at fixed exposure time, and ranges from 13% to about 79% of charged gas with varying exposure time. These findings indicate that exposure time is inherently a more significant driver of lost gas within shale-gas systems than initial saturation pressure. Our observation agrees with published studies pertaining to measuring lost gas, such as investigations of rates associated with pulling core and increasing depths (Seidle, 2011; Hosseini et al., 2015). Core samples could be presumed to experience increased gas loss at longer exposure time during coring, core transport within the borehole, and core handling at the surface. Shale-gas reservoir burial depths are typically an order of magnitude larger than CBM reservoirs, thousands of meters versus hundreds, leading to an increase in the amount of time the sample is exposed to lower pressure conditions during its trip upward (Seidle, 2011; Hosseini et al., 2015).

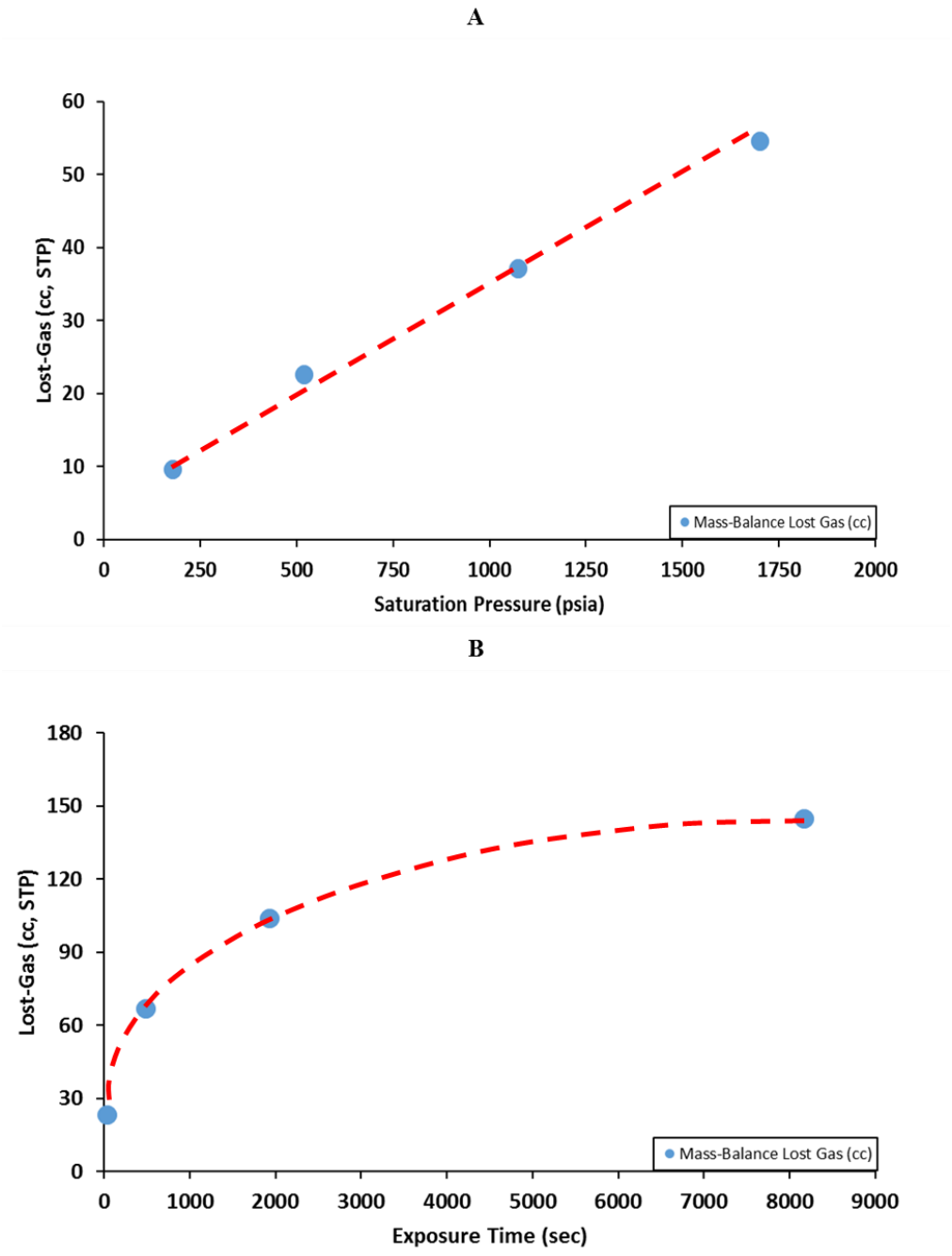

Figure 16. Mass-balance lost gas values in cm3 versus saturation pressure in psia (a) and versus exposure time in seconds (b).

COMPARISON BETWEEN LOST GAS DERIVED FROM MASS-BALANCE APPROACH AND EMPIRICAL METHODOLOGIES

The CBM industry utilizes the extrapolation of a gas-desorption curve gathered from in-the-field canister-desorption measurements to the starting time of desorption, or time zero for lost-gas determination (Mavor and Pratt, 1996; Diamond and Schatzel, 1998; Waechter and Hampton, 2004; Seidle, 2011). These empirical methods include linear extrapolation (Bertard et al., 1970; Kissell et al., 1973; Mavor and Pratt, 1996), nonlinear least-squares extrapolation (Metcalfe et al., 1991; Yee et al., 1993; Shtepani et al., 2010), and polynomial-equation fitting (Waechter and Hampton, 2004).

Linear extrapolation, or the direct method, involves fitting the initial portion of the cumulative-gas-volume curve with a linear equation; the intercept of the extrapolated linear equation at time zero is the lost-gas value. Nonlinear least-squares extrapolation was performed using the methodology, equations, and five associated empirical parameters presented in Shtepani et al. (2010). The least-squares fitting is performed by iterating the Shtepani et al. (2010) Equation 4 until the five empirical parameters converge upon optimized values that minimize the sum of the squared difference between the cumulative-gas volume and the fitted cumulative-gas volume; the fitted intercept was interpreted as the lost-gas value. The polynomial-equation fitting method fit a polynomial function to the entire degassing-cumulative-volume curve, and the intercept was then interpreted as the lost-gas value. Polynomial fitting of a 6th-, 5th-, and 4th-order polynomial was performed (**Figure 17**); the 6th-order polynomial was selected for use owing to its observed closer accuracy to mass-balance lost-gas values.

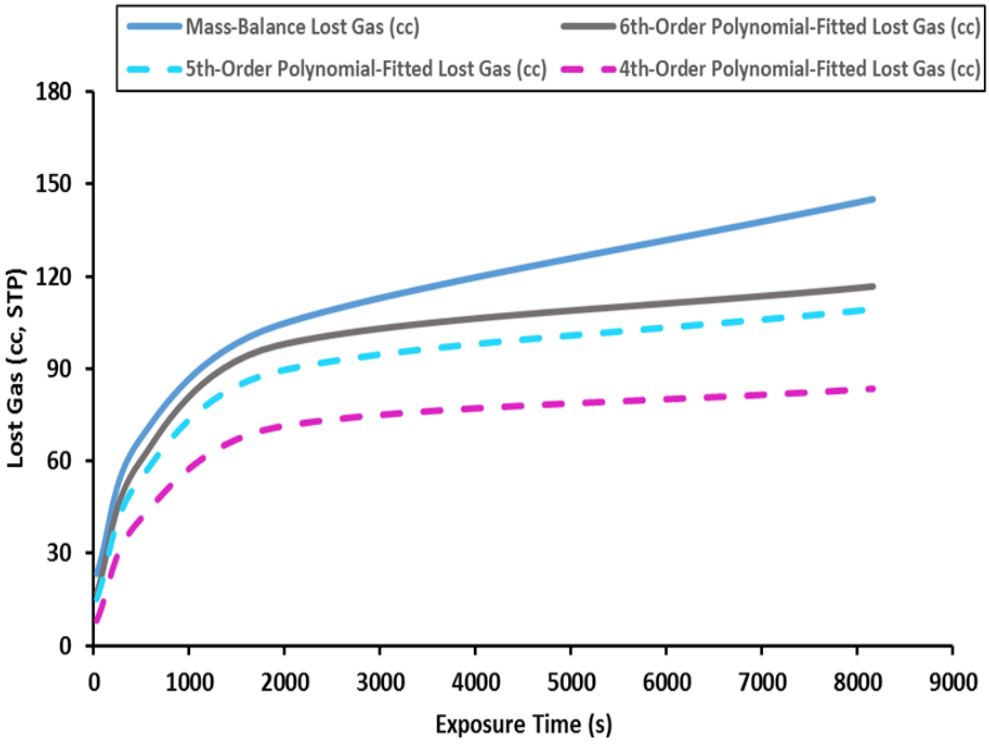

Figure 17. Comparison between mass-balance lost-gas values (blue solid line) and lost-gas values obtained by fitting polynomial equations of different orders, at varying exposure times, at a fixed saturation pressure of 1781.54 Mpa.

The three empirical methods were applied to degassing curves from both sets of experiments; their lost-gas values were determined and compared with the mass-balance lost-gas values (**Figure 18**). Although the three empirical methods achieve a reasonable fit to experimental degassing curves (**Figure 18)**, lost-gas values determined from the intercepts of linear extrapolation, polynomial fitting, and nonlinear least-squares fitting are dramatically different. Therefore, it is reasonable to evaluate the applicability of the three empirical methods to lost-gas estimates from organic-rich shales.

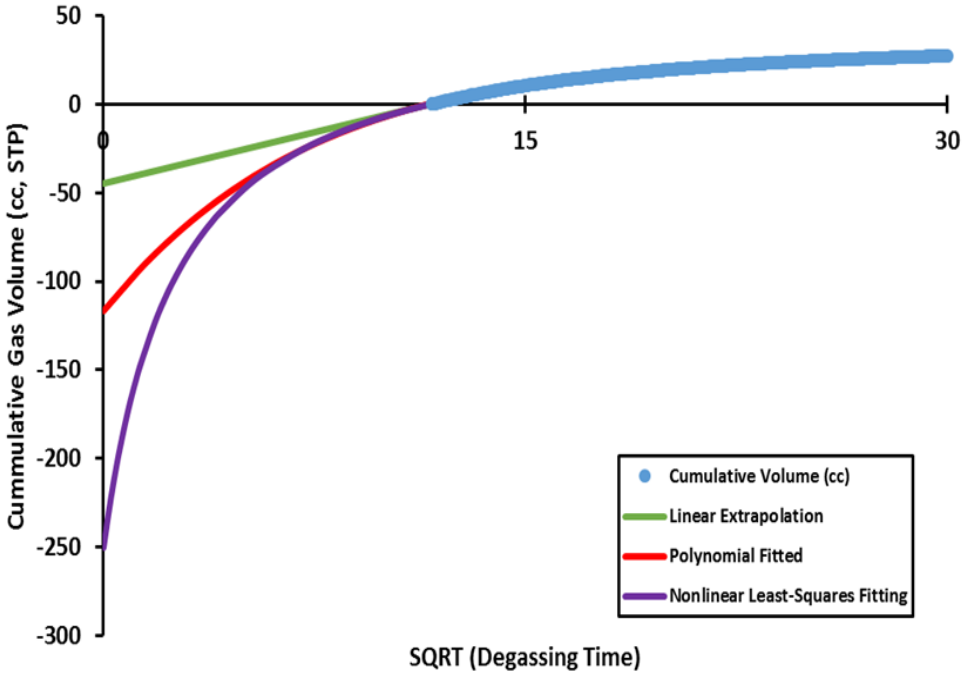

Figure 18. Comparison of lost-gas values (intercepts of three lines) calculated from empirical methods of linear extrapolation, polynomial fitting, and nonlinear least-squares fitting.

The mass-balance lost-gas values were taken as control points, and a direct comparison of empirical and mass-balance lost-gas values from our experiments was made in order to evaluate the applicability of different empirical methods to organic-rich shales (**Figure 19a** and **b**). The nonlinear least-squares fitting lost-gas values were observed to consistently overestimate mass-balance lost gas, whereas linear extrapolation and 6th-order polynomial-fit lost-gas values underestimated the mass-balance lost gas. The longer the exposure time, the greater the difference appears, further suggesting that exposure time is the most significant driver of lost gas. Overall, the 6th-order polynomial

fitting is the most accurate analyzed empirical method for determining lost gas because it deviates the least from mass-balance-derived values when both exposure time and initial saturation pressure are varied.

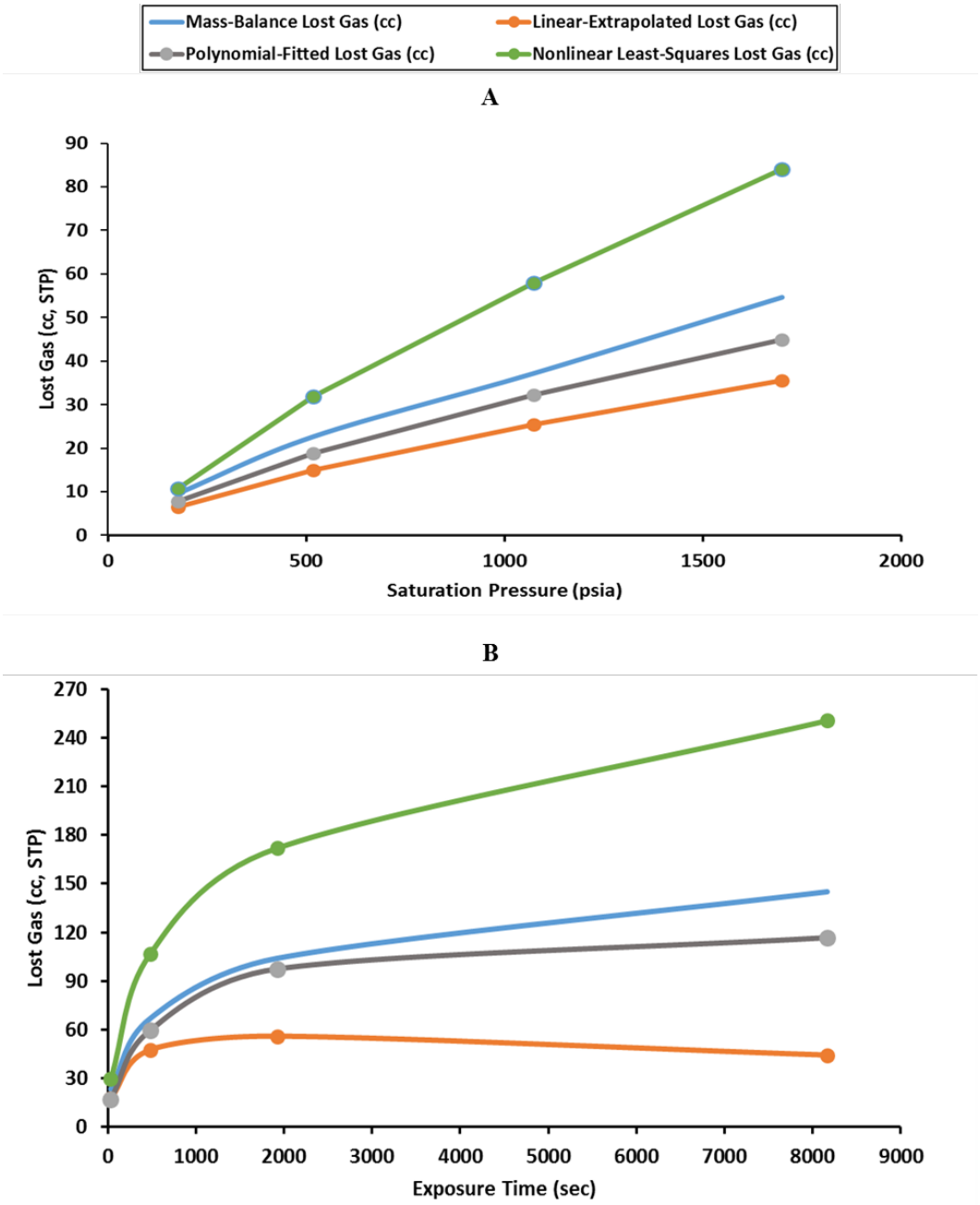

Figure 19. Comparison of mass-balance lost-gas values and lost-gas values obtained by three empirical methods: (a) varied saturation pressure, and (b) varied exposure time.

GAS-IN-PLACE ESTIMATIONS

GIP, for the purposes of this study, is characterized as the sum of lost-gas values, retained-gas values, and gas emitted from the sample values, as shown in **Equation 12**:

$$M_{\text{Gas In Place}} = M_{\text{Emitted,Core Plug}} + M_{\text{Retained,Core Plug}} + M_{\text{Lost}} \quad \text{..... (Equation 12)}$$

where $M_{Gas\ In\ Place}$ = estimated gas originally within samples at reservoir conditions (mmol), $M_{Emitted,\ Core\ Plug}$= total gas emitted from core plugs (mmol), $M_{Retained,\ Core\ Plug}$= total gas retained within core plugs (mmol), and M_{Lost}= total gas lost from samples during exposure conditions, measured by mass-balance or empirical methods (mmol). Retained and emitted gas values can be calculated with the possession of degassing (canister- desorption) curves, pore-volume and headspace (system-volume) values, and gas-adsorption isotherms. GIP values (182 cc) were formulated for mass-balance conditions based on our measured results from experiments with varying exposure time and are considered reference values.

Three GIP values were also estimated based on each empirically estimated lost-gas value derived from experiments with varying exposure time (**Figure 20)**. It is immediately obvious that GIP values derived using the nonlinear least-squares methodology consistently overestimate our mass-balance-derived GIP control points with increasing exposure time; in contrast, a significant underestimation of GIP values derived using both the polynomial fitting and linear-extrapolation methods occurs.

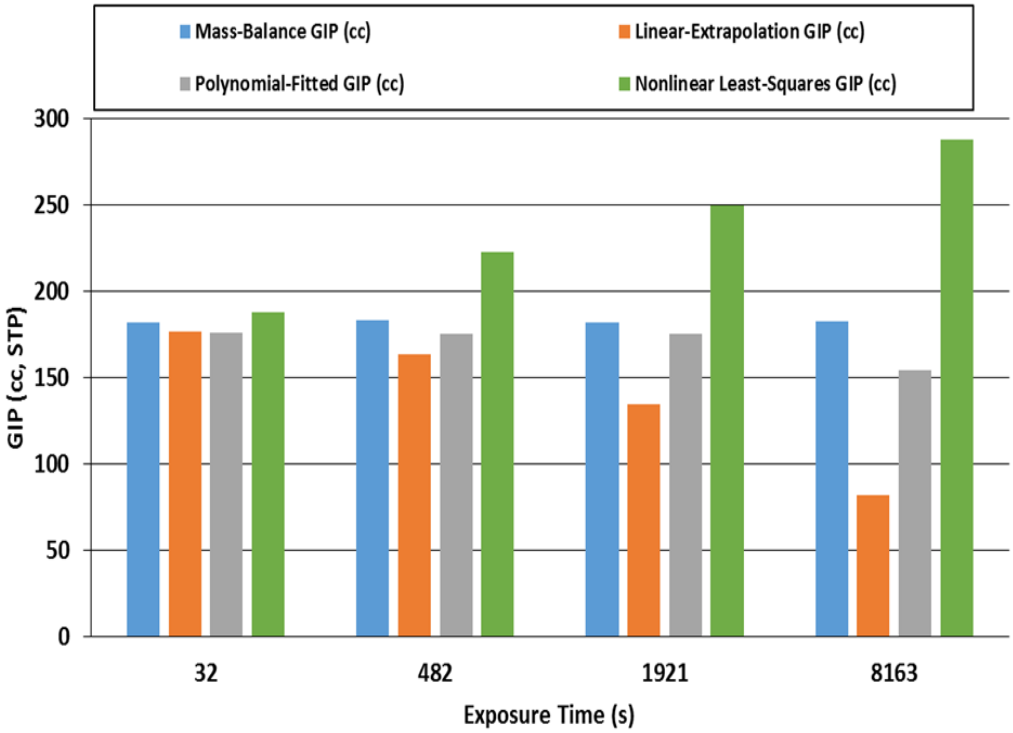

Figure 20. Comparison of Gas-In-Place values obtained by fitting methods and mass-balance calcualtion at varying exposure times and fixed saturation pressure of 1781.54 Mpa.

A quantification of the variance between our mass-balance-derived GIP values and the empirically derived GIP values was performed by a percent-error computation (**Figure 21**). Mass-balance-derived GIP values are considered the reference at 0%; the different empirical GIP values are presented using the same previously mentioned color scheme. As exposure time increases, the percent error ranges from 3% to 58% for the nonlinear least-squares GIP values, from 3% to 55% for the linear extrapolation GIP values, and from 3% to 16% for the polynomial-fitted GIP values. The significantly lower percent-error values for the polynomial-fitting method clearly suggest that it is the most accurate

empirical estimation of GIP with increasing exposure time. Even after an exposure time of over 2 h, the polynomial-fitted GIP values are able to maintain up to 84% accuracy, which far exceeds estimations using the other two empirical methods. The total lost gas during 2 h exposure time takes up 79% of total initially charged gas at resaturation condition. This outcome gives significant support to the previous conclusion that the 6th-order polynomial fitting method is the most accurate empirical methodology for estimating lost gas, under this set of experimental conditions.

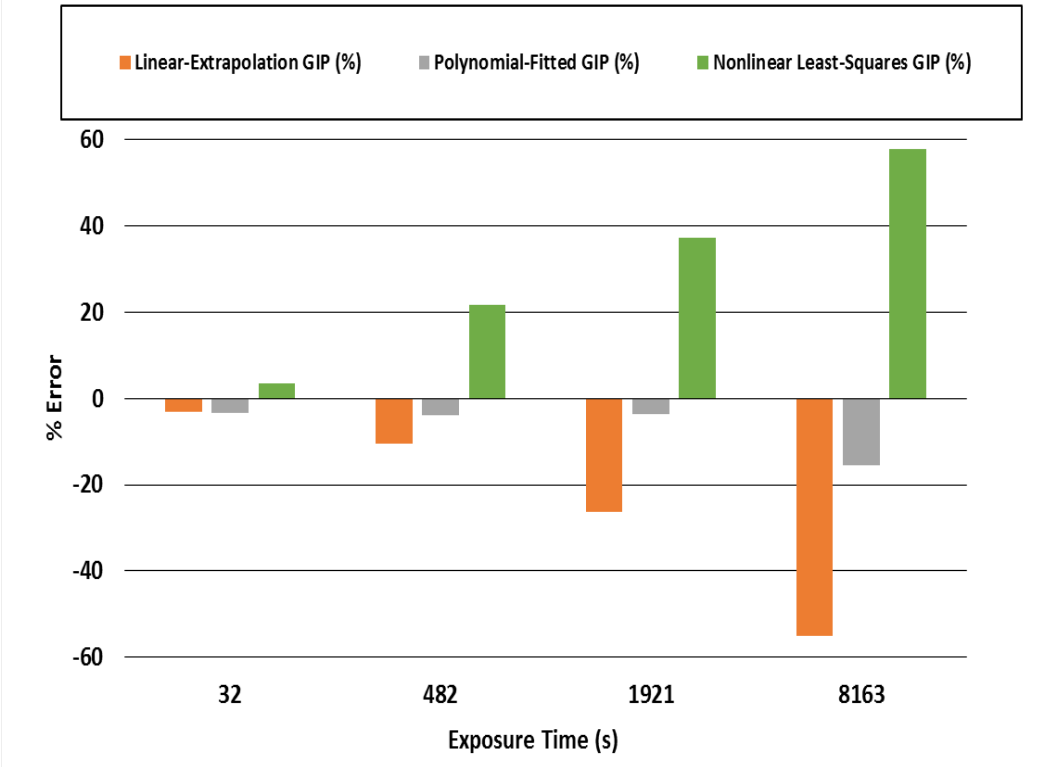

Figure 21. Uncertainty of GIP estimates using three different empirical methods. Mass-balance-derived GIP value used as reference.

Chapter 6: Future Work

Several variables and assumptions that have marked effects on, and possible implications for, lost gas should be taken into consideration, such as the effect of drilling conditions, scaling up, and real-world sample conditions. The 1-inch OD core plug was sampled, along with the 3/8-inch OD core plugs used in this study, with the intention of determining the effects of core-plug diameter on lost-gas values. The scope of this work did not permit performing the entire experimental method on a 1-inch OD plug because of the estimated equilibration time—weeks to months—required. This method of upscaling lost-gas results to full-sized industry-standard samples should be further investigated. Shale-gas wells are drilled using drilling mud and, depending on drilling practices, can provide a hydrostatic pressure regime equivalent to, beyond, or below reservoir pressure (Diamond and Schatzel, 1998). With this in mind, samples could possibly retain in situ gas for a significant fraction of the trip up the borehole; several lost-gas estimation methodologies assume that gas loss commences halfway up the borehole for this reason (Kissell et al., 1973; Diamond and Schatzel, 1998).

The variation in external pressure conditions the samples are subjected to, both in scale and timing, should be quantified in further work. Lithostatic pressure from the overburden should also be kept in mind, and further works should be attempted by placing samples under confining pressure in order to more accurately simulate in situ conditions. Temperature, which varies significantly within the borehole between reservoir and surface conditions, has to be taken into consideration because it can have a major effect on lost gas (Mavor and Pratt, 1996; Seidle, 2011). This variation in

temperature, as well as the variation of temperature through time, can possibly lead to increases and decreases in the rate of gas loss and should be examined. Ultra-high pressures, up to 6,000 psi, that can be observed in shale-gas reservoirs (Hosseini et al., 2015) must also be accounted for; this work only observes a small window of initial saturation pressures between approximately 200 and 1,800 psi.

Chapter 7: Conclusions

A CH_4-resaturatution and degassing experimental method was developed to re-create the types of pressure conditions experienced by shale-gas core samples during coring, transport, handling, and degassing. The degassing curve at different exposure times provides key insight into the different physiochemical mechanisms that drive gas loss in the organic-rich Barnett Formation under isothermal conditions. A combination of gas expansion from pore volume and gas desorption from pore surfaces affects the shape of the degassing curve. Gas expansion is observed to dominate in the early stages of degassing, and gas desorption is recognized to progressively dominate in the late stages. Exposure time, or the amount of core transport and handling time, is a more significant driver of gas loss than initial gas-saturation pressure, or the amount of gas originally contained within the samples, suggesting that effective and economic steps must be taken to limit transport and handling time as much as possible to more accurately measure GIP. The application of various empirical methodologies for estimating lost gas taken from the CBM industry was evaluated by direct comparison to mass-balance-derived lost-gas values; results reveal that the polynomial equation fitting of isothermal degassing curves is a viable way to estimate lost gas. This specific empirical method is shown to estimate lost gas, and more importantly GIP, with up to 85% accuracy when about 79% of initial gas was lost.

References

Ambrose, R.J., R.C. Hartman, M. Diaz-Campos, I.Y. Akkutlu, and C.H. Sondergeld. 2010. New Pore-scale Considerations for Shale Gas in Place Calculations. SPE Unconventional Gas Conference, Pittsburgh, Penn., 23-25 February. SPE-131772-MS.

Arbenz, J.K. 1989. The Ouachita system. In: Bally, A.W., and A.R. Palmer (Eds.), The geology of North America—An overview: Geological Society of America, The Geology of North America, vol. A, p. 371–396.

Bertard, C., B. Bruyet, and J. Gunther. 1970. Determination of desorbable gas concentration of coal (direct method). Int. J. Rock Mech. Mining Sci. & Geomechanics Abs. 7 (January): 43–65, IN3–IN4, 51–65.

Blakey, R. 2005. Paleogeography and geologic evolution of North America: Images that track the ancient landscapes of North America: http://www.jan.ucc.nau.edu/rcb7/namM325.jpg (Accessed: March 1, 2017).

Bowker, K.A. 2003. Recent developments of the Barnett Shale play, Fort Worth Basin. West Tex. Geo. Soc. Bull., vol. 42, p. 4–11.

Browning, J., S. Ikonnikova, G. Gülen, and S. Tinker. 2013. Barnett Shale Production Outlook. SPE Economics & Management, vol. 5(03), p. 89–104. SPE-165585-PA.

Carslaw, H.S., and J.C. Jaeger. 1959. Conduction of Heat in Solids, 2nd ed. Oxford University Press, London, United Kingdom. 510 p.

Cheney, M.G. 1940. Geology of north-central Texas, AAPG Bull., vol. 24 (1), p. 65–118.

Crank, J. 1956. The Mathematics of Diffusion. Oxford University Press, London, United Kingdom. 347 p.

Cui, X., A.M.M. Bustin, and R.M. Bustin. 2009. Measurements of gas permeability and diffusivity of tight reservoir rocks: Different approaches and their applications. Geofluids, vol. 9, p. 208–223.

Cui, X., and R.M. Bustin. 2010. A New Method to Simultaneously Measure In-Situ Permeability and Porosity under Reservoir Conditions: Implications for Characterization of Unconventional Gas Reservoirs. Petroleum Conference, Calgary, Alberta, Canada. 19–21 October.

Diamond, W. P., and S.J. Schatzel. 1998. Measuring the gas content of coal: A review. Int. J. of Coal Geol., vol. 35(1–4), p. 311–331.

Do, D.D., and H.D. Do. 2003. Adsorption of supercritical fluids in non-porous and porous carbons: Analysis of adsorbed phase volume and density. Carbon, vol. 41, p. 1777–1791.

Dunham, R.J. 1962. Classification of carbonate rocks according to depositional texture, in Ham, W.E., ed., Classification of Carbonate Rocks: AAPG Memoir 1, p. 108–121.

Energy Information Administration (EIA) 2015. Top 100 U.S. Oil and Gas Fields, March 2015. https://www.eia.gov/naturalgas/crudeoilreserves/top100/pdf/top100.pdf (Accessed: March 1, 2017).

Energy Information Administration (EIA) 2017. Annual Energy Outlook 2017: With projections to 2050, Jan. 2017. https://www.eia.gov/outlooks/aeo/pdf/0383(2017).pdf (Accessed: March 1, 2017).

Etminan, S.R., F. Javadpour, B.B. Maini, and Z. Chen. 2013. Measurement of gas storage processes in shale and of the molecular diffusion coefficient in kerogen. Int. J. Coal Geol., vol. 123, p. 10–19.

Etminan, S.R., B.B. Maini, Z. Chen, and H. Hassanzadeh. 2010. Constant-pressure technique for gas diffusivity and solubility measurements in heavy oil and bitumen. Energy & Fuels, vol. 24(1), p. 533–549.

Etminan, S.R., M. Pooladi-Darvish, B.B. Maini, and Z. Chen. 2012. Modeling the interface resistance in low soluble gaseous solvents-bitumen systems. Fuel, vol. 105, p. 672–687.

Fu, Q., S.C. Horvath, E.C. Potter, F. Roberts, S.W. Tinker, S. Ikonnikova, W.L. Fisher, and J. Yan. 2015. Log-derived thickness and porosity of the Barnett Shale, Fort Worth basin, Texas: Implications for assessment of gas shale resources. AAPG Bull., vol. 99(01), p. 119–141.

Gasparik, M., P. Bertier, Y. Gensterblum, A. Ghanizadeh, B.M. Krooss, and R. Littke. 2014. Geological controls on the methane storage capacity in organic-rich shales. Int. J. of Coal Geol., vol. 123(C), p. 34–51.

Gasparik, M., A. Ghanizadeh, P. Bertier, Y. Gensterblum, S. Bouw, and B.M. Krooss. 2012. High-pressure methane sorption isotherms of black shales from the Netherlands. Energy & Fuels, vol. 26, p. 4995–5004.

Gensterblum, Y., P. van Hemert, P. Billemont, A. Busch, D. Charriére, D. Li, B.M. Krooss, G. deWeireld, D. Prinz, and K-H.A.A. Wolf. 2009. European inter-laboratory comparison of high pressure CO_2 sorption isotherms I: Activated carbon. Carbon, vol. 47, p. 2958–2969.

Gensterblum, Y., P. van Hemert, P. Billemont, A. Busch, D. Charriére, D. Li, B.M. Krooss, G. deWeireld, D. Prinz, and K-H.A.A. Wolf. 2010. European inter-laboratory comparison of high pressure CO_2 sorption isotherms I: Activated carbon. Int. J. Coal Geol., vol. 84, p. 115–124.

Goodman, A.L., A. Busch, G.J. Duffy, J.E. Fitzgerald, K.A.M. Gasem, Y. Gensterblum, B.M. Krooss, J. Levy, E. Ozdemir, Z. Pan, R.L. Robinson, K. Schroeder, Jr., M. Sudibandriyo, and C. White. 2004. An inter-laboratory comparison of CO_2 isotherms measured on Argonne premium coal samples. Energy & Fuels, vol. 18, p. 1175–1182.

Gregg, S.J., and K.S.W. Sing. 1982. Adsorption, Surface Area and Porosity, 2nd ed. Academic Press, New York.

Gutschick, R., and C. Sandberg. 1983. Mississippian continental margins on the conterminous United States. In: Stanley, D.J., and G.T. Moore (Eds.), The shelf break: Critical interface on continental margins: SEPM Special Publication, vol. 33, p. 79–96.

Handwerger, D.A., D.M. Willberg, M. Pagels, B. Rowland, and J. Keller. 2012. Reconciling retort versus Dean Stark measurements on tight shales. SPE Annual Technical Conference and Exhibition, San Antonio, TX., 8-10 October. SPE-159976-MS.

Haugen, K.B., and A. Firoozabadi. 2009. Mixing of two binary nonequilibrium phases in one dimension. AlChE J, vol. 55(8), p. 1930–1936.

Hosseini, S. A., F. Javadpour, and G.E. Michael. 2015. Novel analytical core-sample analysis indicates higher gas content in shale-gas reservoirs. SPE Journal, vol. 20(06), p. 1,397–1,408. SPE-174549-PA.

Hu, H., T. Zhang, J.D. Wiggins-Camacho, G.S. Ellis, M.D. Lewan, and X. Zhang. 2015. Experimental investigation of changes in methane adsorption of bitumen-free Woodford Shale with thermal maturation induced by hydrous pyrolysis. Marine and Petrol. Geol., vol. 59(c), p. 114–128.

Hyland, C.R. 1983. Pressure Coring-An Oilfield Tool. SPE Annual Technical Conference and Exhibition, San Francisco, Ca., 5-8 October. SPE-12093-MS.

Jarvie, D.M., B.L. Claxton, F. Henk, and J.T. Breyer. 2001. Oil and shale gas from the Barnett Shale, Ft. Worth Basin, Texas, AAPG National Convention, June 3–6, Denver, Colo., AAPG Bull., vol. 85, no. 13 (Supplement), p. A100.

Jarvie, D.M., R.J. Hill, and R.M. Pollastro. 2005. Assessment of the gas potential and yields from shales: The Barnett Shale Model. In: Cardott, B.J. (Ed.), Unconventional energy resources in the southern Midcontinent, 2004 symposium: Oklahoma Geological Survey Circular 110, p. 37–50.

Jarvie, D.M., R.J. Hill, R.M. Pollastro, D.A. Wavrek, K.A. Bowker, B.L. Claxton, and M.H. Tobey. 2003. Evaluation of unconventional natural gas prospects: The Barnett Shale fractured shale model (abs.): 21st International Meeting on Organic Geochemistry, September 8-12, Krakow, Poland, Book of Abstracts, Part II, p. 3–4.

Jarvie, D.M., R.J. Hill, T.E. Ruble, and R.M. Pollastro. 2007. Unconventional shale-gas systems: The Mississippian Barnett Shale of north-central Texas as one model for thermogenic shale-gas assessment. AAPG Bull., vol. 91(4), p. 475–499.

Javadpour, F. 2009. Nanopores and apparent permeability of gas flow in mudrocks (shales and siltstone). J. Can. Pet. Technol., vol. 48, p. 16–21.

Javadpour, F., D. Fisher, and M. Unsworth. 2007. Nanoscale gas flow in shale gas sediments. J. Can. Pet. Technol., vol. 46, p. 55–61. SPE-071006-PA.

Keller, J.U., and R. Staudt. 2005. Gas Adsorption Equilibria: Experimental Methods and Adsorption Isotherms. Springer, New York, 422 p.

Kissell, F.N., C.M. McCulloch, and C.H. Elder. 1973. The Direct Method of Determining Methane Content of Coalbeds for Ventilation Design. Report of Investigations 7767, U.S. Bureau of Mines, Washington, D.C.

Krooss, B.M., F. van Bergen, Y. Gensterblum, N. Siemons, H.J.M Pangier, and P. David. 2002. High pressure CH_4 and carbon dioxide adsorption on dry and moisture equilibrated Pennsylvanian coals. Int. J. of Coal Geol., vol. 51, p. 69–92.

Langmuir, I. 1918. The adsorption of gases on plane surfaces of glass, mica and platinum. J. Am. Chem., vol. 40(9), p.1361-1403.

Loucks, R.G., R.M. Reed, S.C. Ruppel, and D.M. Jarvie. 2009. Morphology, genesis, and distribution of nanometer-scale pores in siliceous mudstones of the Mississippian Barnett Shale. J. Sed. Research, vol. 79(12), p. 848–861.

Loucks, R.G., and S.C. Ruppel. 2007. Mississippian Barnett Shale: Lithofacies and depositional setting of a deep-water shale-gas succession in the Fort Worth Basin, Texas. AAPG Bull., vol. 91, p. 579–601.

Lu, X.C., F.C. Li, and A.T. Watson. 1995. Adsorption measurements in Devonian shales. Fuel, vol. 47, p. 599–603.

Mavor, M.J., L.B. Owen, and T.J. Pratt. 1990. Measurement and Evaluation of Coal Sorption Isotherm Data. SPE 65th Annual Technical Conference and Exhibition of Petroleum Engineers, New Orleans, La., p.157–170. September 23–36. SPE-20728-MS.

Mavor, M.J., J.S. Close, and R.A. McBane. 1994. Formation Evaluation of Exploration Coalbed-Methane Wells. SPE Formation Evaluation, vol. 9(4), p. 285–294. SPE-21589-PA.

Mavor, M.J., and T.J. Pratt. 1996. Improved methodology for determining total gas content, vol. II: Comparative evaluation of the accuracy of gas-in-place estimates and review of lost gas models. Gas Research Inst., Topical Rep. GRI-94/0429.

McCarty, R.D., and V.D. Arp. 1990. A new wide range equation of state for helium. Adv. In Cryog. Eng., vol. 35, p. 1465–1475.

McLennan, J.D., P.S. Schafer, and T.J. Pratt. 1995. A Guide to Determining Coalbed Gas Content. Gas Research Inst., Topical Rep. GRI-94/0396.

Metcalfe, R.S., D. Yee, J.P. Seidle, and R. Puri. 1991. Review of Research Efforts in Coalbed Methane Recovery. SPE Asia-Pacific Conference, Perth, Western Australia, p. 727–740. November 4–7. SPE-23025-MS.

Milliken, K.L., M. Rudnicki, D.N. Awwiller, and T. Zhang. 2013. Organic matter–hosted pore system, Marcellus Formation (Devonian), Pennsylvania. AAPG Bull., vol. 97(2), p. 177–200.

Montgomery, S.L., D.M. Jarvie, K.A. Bowker, and R.M. Pollastro. 2005. Mississippian Barnett Shale, Fort Worth basin, north-central Texas: Gas-shale play with multi–trillion cubic foot potential. AAPG Bull., vol. 89(2), p. 155–175.

Mullane, J.J. 1941. Pressure Core Analysis. API Drilling and Production Practice, New York, NY, 1 January. API-41-163.

Murata, K., M. El-Merraoui, and K. Kaneko. 2001. Absolute adsorption isotherm of supercritical gases. J. of Chem. Phys., vol. 114(9), p. 4196–4205.

Peng, S., and R.G. Loucks. 2016. Permeability measurements in mudrocks using gas-expansion methods on plug and crushed-rock samples. Marine and Petrol. Geol., vol. 73, p. 299–310.

Plummer, F.B. 1950. The Carboniferous rocks of the Llano region of central Texas, University of Texas Bull., vol. 4329, p. 1–170.

Pollastro, R.M., D.M. Jarvie, R.J. Hill, and C.W. Adams. 2007. Geologic framework of the Mississippian Barnett Shale, Barnett-Paleozoic total petroleum system, Bend arch–Fort Worth Basin, Texas. AAPG Bull., vol. 91(4), p. 405–436.

Railroad Commission of Texas (RRC) 2017. Natural Gas Production and Well Counts (since 1935), History of Texas Initial Natural Gas, Annual Production and Producing Wells, April 21, 2016. http://www.rrc.state.tx.us/oil-gas/research-and-statistics/production-data/historical-production-data/natural-gas-production-and-well-counts-since-1935/ (Accessed: March 1, 2017).

Riazi, M.R. 1996. A new method for experimental measurement of diffusion coefficients in reservoir fluids. J. Pet. Sci. Eng., vol. 14(3-4), p. 235–250.

Rowe, H.D., R.G. Loucks, S.C. Ruppel, S.M. Rimmer. 2008. Mississippian Barnett Formation, Fort Worth Basin, Texas: Bulk geochemical inferences and Mo–TOC constraints on the severity of hydrographic restriction. Chem. Geol., vol. 257, p. 16–25.

Seidle, J. 2011. Fundamentals of Coalbed Methane Reservoir Engineering. Tulsa, Oklahoma: PennWell Corporation, p. 93–124.

Setzmann, U., W. Wagner, and A. Pruss. 1991. A new equation of state and tables of thermodynamic properties for methane covering the range from the melting line to 625 K at pressures up to 1000 Mpa. J. of Phys. and Chem. Ref. Data, vol. 20, p. 1061–1151.

Shtepani, E., L.A. Noll, L.W. Elrod, and P.M. Jacobs. 2010. A new regression-based method for accurate measurement of coal and shale gas content. SPE Res. Eval. & Eng., vol. 13(2), p. 359–364. SPE-115405-PA.

Sircar, S. 1999. Gibbsian surface excess for gas adsorption–revisited. Ind. Eng. Chem. Res., vol. 38, p. 3670–3682.

United States Geological Survey (USGS). 2015. USGS Estimates 53 Trillion Cubic Feet of Gas Resources in Barnett Shale, December 17, 2015. https://www.usgs.gov/news/usgs-estimates-53-trillion-cubic-feet-gas-resources-barnett-shale (Accessed: March 1, 2017).

Waechter, N.B., and G.L. Hampton III. 2004. Overview of coal and shale gas measurement: Field and laboratory procedures in 2004 International Coalbed Methane Symposium. The University of Alabama, Tuscaloosa. p. 1–17.

Walper, J.L. 1982. Plate tectonic evolution of the Fort Worth Basin. In: Martin, C.A. (Ed.) Petroleum Geology of the Fort Worth Basin and Bend Arch Area. Dallas Geological Society, p. 237–251.

Yee, D., J.P. Seidle, and W.B. Hanson. 1993. Gas sorption on coal and measurement of gas content. In: Law, B.E., and D.D. Rice (Eds.), Hydrocarbons from Coal. Am. Assoc. Pet. Geol., Tulsa, Okla., p. 159–184.

Zhang, T., G.S. Ellis, S.C. Ruppel, K. Milliken, and R. Yang. 2012. Effect of organic-matter type and thermal maturity on methane adsorption in shale-gas systems. Org. Geochem., vol. 47, p. 120–131.

Zhang, T., and B.M. Krooss. 2001. Experimental investigation on the carbon isotope fractionation of methane during gas migration by diffusion through sedimentary rocks at elevated temperature and pressure. Geochimica Et Cosmochimica Acta, vol. 65(16), p. 2723–2742.